

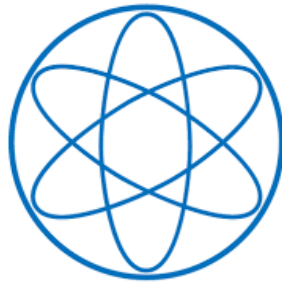
TECHNICAL UNIVERSITY OF MUNICH
PHYSICS DEPARTMENT

BACHELOR'S THESIS IN NUCLEAR AND PARTICLE PHYSICS

Investigation of high voltage contacts on high purity germanium detectors for LEGEND

Untersuchung von Hochspannungskontakten an Germanium Detektoren
für LEGEND

Bogdan Gheorghe Gulie
Matriculation number: (03746105)



PHYSIK
DEPARTMENT

Supervisor: Prof. Dr. ret. nat. Susanne Mertens
Responsible advisors: Dr. Konstantin Gusev, Dr. ret. nat. Michael
Willers, MSc. Florian Henkes

1 Abstract

The world of elementary particles always presented itself as a difficult area of physics, challenging our understanding about the way our Universe is built. Starting with the discovery of subatomic particles and quantum physics, the view about our world changed forever and the quest for grasping full knowledge on the mechanism of particles became a quest for many physicists.

The LEGEND collaboration sets ambitious goals for physics, challenging the fundamental theories about the smallest building blocks of matter, the elementary particles. Neutrinos are ones of them, which impose many questions and unknown mechanisms until today. They are elusive, very light so that their mass was not measured yet and interact mostly nuclear weakly. On top of that, neutrinos also oscillate from one family to another. Properties of neutrinos are tested with a huge set up beneath the Gran Sasso mountains, where hopes for Ettore Majorana's theory are alive. Namely, that with a small chance in ^{76}Ge isotope, where double beta decays happen, one will detect the first nuclear decay, where two neutrinos would have an exchange interaction and not be emitted in the end. The exact interaction is not known and it is often described as a black box in Feynman diagrams. If this reaction were found, it would prove that Majorana's theory was right. His theory displayed neutrinos as particles which are identical to their own anti-particles, like the photon. The sought new nuclear decay would be therefore called neutrinoless double beta decay. LEGEND is an experiment with more ambitious plans, because if the new decay is detected, one could make statements about the mass ordering and rest mass of the neutrino.

In this thesis technical problems of the germanium detectors are researched, because they represent a hurdle in the operational process of the detectors needed for discovery. Since performance problems have been observed at several detectors in LEGEND-200 during calibration tests, it was considered that some of them were caused by the bad quality of the high voltage contacts. The performance problems observed regard the change of the peak and pulser positions for a gamma radiation spectrum in high voltage scans performed in argon. Although germanium detectors have been used for radiation detection for more than half a century, a test for the high voltage contacts is well motivated by this problem. Therefore, the decision to analyse the response of the germanium detector with different types of high voltage contacts on a calibration run using liquid nitrogen at cryogenic temperatures in the laboratory is a first step in understanding what hinders a germanium detector to maintain its full ability of excellent energy resolution.

Contents

1	Abstract	1
2	Introduction	3
3	Neutrino physics	3
3.1	Discovery of the neutrino	3
3.2	Neutrino mass	5
3.2.1	Neutrino oscillations	5
3.2.2	Methods to determine the neutrino mass	5
3.3	Neutrinoless double beta decay ($0\nu\beta\beta$)	6
4	LEGEND experiment	9
4.1	LEGEND-200	10
4.2	LEGEND-1000	12
4.3	Detector types used in LEGEND-200	12
5	Experimental techniques	15
5.1	Semiconductor detectors	15
5.1.1	Bandgap structure	15
5.1.2	Doping	16
5.1.3	Working principle of semiconductor detectors	18
5.2	Electronics and charge sensitive amplifier	18
6	Test of different high voltage contacts	20
6.1	Observed issues and possible explanation	20
6.2	Experimental setup	24
7	Resistance measurements on the contacts	27
8	Spectroscopy analysis	33
8.1	Analysis of waveforms	33
8.2	Analysis on contacts	41
8.2.1	Aluminium contact	46
8.2.2	Lithium contact	48
8.2.3	Polished lithium contact	51
8.2.4	Comparison between contacts	53
9	Conclusion and outlook	56

2 Introduction

The goal of this thesis is to start an experimental test regarding the influence of the high voltage contacts on the performance of a germanium detector, in order to see if there exists a relationship between the quality of the contact and performance of the detector, for example the signal amplitude and the energy resolution.

The thesis starts with a short introduction in the world of elementary particle physics, focusing on the main properties of the particles called neutrinos. Then, it will address the main questions in the field of neutrino research, like the mass measurement methods and the search for a hypothetical radioactive decay, called the neutrinoless double beta decay.

Further, the LEGEND experiment will be described in a brief introduction, as it is a way of researching the existence of the neutrinoless double beta decay. The next chapter is dedicated to the experimental method and working principle of semiconductor detectors, which are of paramount importance in radiation detection. The current motivation for the tests on the high voltage contacts will be explained in a more detailed fashion, followed by the measurements, analysis procedures and results obtained.

3 Neutrino physics

Neutrinos are light particles included also in the Standard Model as massless objects, present only through gravitational and weak interaction. The Standard Model of particle physics classifies all elementary particles and their interaction forces (gravitational, electromagnetic, strong nuclear and weak nuclear). The particles are either fermions (such as the electron and the neutrino) or gauge bosons for each interaction excepting gravity (the photon, the W, Z bosons and gluons). Furthermore, the fermions are divided in families (electronic, muonic, tauonic)[1].

Since their discovery, neutrinos have been puzzling objects for physicists, because their unexpected behaviour has led to more questions and still unsolved problems. Since neutrino oscillations have been discovered, it was understood that neutrinos must have a mass. The argument that stands for the existence of a non zero neutrino mass lies in the ability of the neutrino to oscillate from one flavour to another.

3.1 Discovery of the neutrino

The neutrino was postulated by Wolfgang Pauli [2], trying to explain the distortion observed in the spectra of beta decays and conservation of momentum, energy and spin. This distortion is presented in figure 1, where there can be seen how the energy is distributed and not localized at a single point. The standard beta decay of an isolated neutron is presented in the first equation:



where a neutron decays into a proton, an electron and an anti-electron neutrino. On both sides of the reaction, energy, spin and momentum must be conserved. As lepton number is also conserved, it will be found out that the third particle will be of antimatter, namely the electron antineutrino.

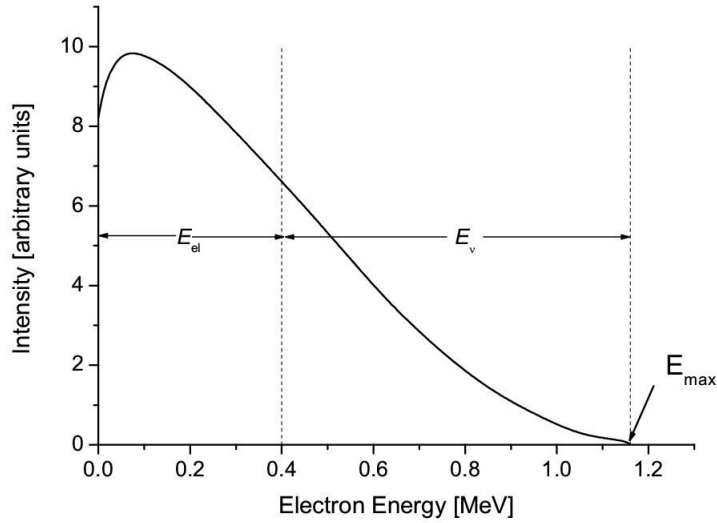


Figure 1: Spectrum of electrons in beta decay: the energy is not collected only by the electron, but distributed over the spectrum, because of the emission of a third particle, namely the electron antineutrino [3]

The first experimental proof came years later, in 1956 by Clyde Cowan and Frederick Reines during the Poltergeist project [4]. This consisted in the capture of neutrinos originating from a nuclear reaction redirected on a target of water enriched with cadmium chloride (CdCl_2). Therefore, antineutrinos were caught on neutrons, in an inverse beta decay:



resulting in a production of positrons, which annihilated with the electrons, producing a gamma signal. The second gamma signal came from the de-excitation of cadmium, while the timestamp between the two signals was the confirmation coincidence signal for the presence of the neutrino.

The research continued by discovering two additional flavour eigenstates of the neutrino, corresponding to the heavier partners of the electron, namely muon and tauon neutrino. The muon neutrino was discovered at the Brookhaven National Laboratory in 1962 [5]. The idea of the experiment was to collide a beam of energetic protons from the synchrotron on a target of beryllium. Thus, pion particles would be produced, which will rapidly decay into muons and muon neutrinos [5]. Then, the neutrinos were detected in a spark chamber. For production of the tau neutrino, much higher energies were needed. The discovery was announced in 2000 by the DONUT collaboration at the Fermilab in the United States after colliding even more energetic proton beams with the target [6]. The mechanism is similar to the muon neutrino, as charmed mesons are formed which then decay into the tau neutrino. At Fermilab the detector was formed by a lead shielding, a scintillator and emulsion sheet layers [7].

3.2 Neutrino mass

3.2.1 Neutrino oscillations

The solar neutrino problem remained for years an intriguing unsolved problem. The flux of electron neutrinos produced during nuclear fusion in the sun can be calculated within the assumptions of the Standard Solar model, in the simple proton proton chain model. The problem concerned the large discrepancy between the flux of solar neutrinos calculated from the sun's luminosity and the one measured in detector experiments, such as Homestake or Kamiokande [8]. The hypothesis that the neutrino flavour could oscillate and change while propagating was confirmed by the SNO experiment, which measured fluxes of neutrinos in different scattering processes (namely charged and neutral current interactions or elastic scattering) [1]. The result confirmed the fact that neutrinos are oscillating and transmuting from one flavour eigenstate to another. This implies directly that they also have a mass. The probability that a neutrino oscillates from one flavour to another is given by the following formula [1]:

$$P(\nu_e \longrightarrow \nu_\mu) \approx 1 - \sin^2(2 \cdot \theta_{12}) \cdot \sin^2\left(2 \cdot \Delta m_{12} \cdot \frac{L}{4E}\right) \quad (3)$$

where the θ_{12} represents the mixing angle between the two flavour eigenstates, Δm_{12} the absolute mass difference between the two mass eigenstates, L the length and E the energy of the neutrino beam [1]. The neutrino oscillation results from the mixing of the mass (ν_1, ν_2, ν_3) and flavor eigenstates (ν_e, ν_μ, ν_τ) of the neutrinos. The mass eigenstates are the eigenvalues of the Hamiltonian for propagating in vacuum. These two sets of eigenstates are not identical, but can be related by the Pontecorvo-Maki-Nakagawa-Sakata (PMNS) matrix U [1], which describes the mixing between mass and flavour eigenstates:

$$\begin{pmatrix} \nu_e \\ \nu_\mu \\ \nu_\tau \end{pmatrix} = \begin{pmatrix} U_{e1} & U_{e2} & U_{e3} \\ U_{\mu1} & U_{\mu2} & U_{\mu3} \\ U_{\tau1} & U_{\tau2} & U_{\tau3} \end{pmatrix} \cdot \begin{pmatrix} \nu_1 \\ \nu_2 \\ \nu_3 \end{pmatrix} \quad (4)$$

This mixing can be understood as a rotation in a three dimensional space between the eigenstates.

3.2.2 Methods to determine the neutrino mass

There are several experimental approaches to measure or estimate the neutrino mass. However, until nowadays all experiments only yield an upper limit for the neutrino mass. Two important ways are the direct mass measurements via spectroscopy and the measurement in cosmology.

- Through cosmological models

The most widespread cosmological model, the Lambda cold dark matter model tries to explain the foundations of our Universe and evolution. The main assumptions are the origin of the Universe in the Big Bang explosion and a structural composition of baryonic matter, dark matter and dark energy. Observations of the cosmic microwave background (CMB) combined with Lyman-alpha forest provide an upper limit on the sum over all neutrino mass eigenstates of [9]

$$m_\nu = \sum_i m_i < 0.12eV \quad (5)$$

The main concern lies in the big number of model assumptions and its dependence.

- Direct mass measurement

The KATRIN experiment aims to determine the mass of the electron antineutrino, by using a massive electron spectrometer with a MAC-E filter (Magnetic Adiabatic Collimation combined with an Electrostatic Filter) [10] to measure the decay kinematics of tritium. Tritium undergoes the following beta decay:



This will take into consideration the spectrum of the highly energetical electrons. The kinematic energy spectrum of the electron is of interest as it gives access to the squared effective mass of the neutrino: m_{ν}^2 . Currently, the most recent campaign yielded an upper mass limit of:

$$m_{\bar{\nu}_e} < 0.80\text{eV} \quad (7)$$

at 90 percent confidence level [11].

- Neutrinoless double beta decay

In this case, a mono-energetic peak at the kinematic end-point of the double beta decay corresponding continuous spectrum is observed as the two neutrinos created in that decay would annihilate by an exchange reaction immediately before leaving the nucleus. Current best upper limits are calculated by the GERDA and KAMLAND-ZEN experiment, lying at $m_{\beta\beta} < 79 - 180$ meV [12]. This method of direct measurement is beneficial as it is model-independent.

There are several reasons to investigate if the neutrino is indeed its own antiparticle (a Majorana fermion). The Majorana fermion needs to have a mass (in order to be different from a Dirac fermion) and be a spin 1/2 particle (in order to satisfy the Dirac equation). When looking through the perspective of the wavefunction formalism, the Majorana spinor has the intriguing property that the charge conjugate of the spinor is the spinor itself, meaning that the particle is its own antiparticle. This comes in opposition to the Dirac spinor with four components, where the particle and antiparticle are distinct [13]. Since the neutrino is a spin 1/2 particle and also has a mass confirmed by its flavour oscillations, the verification of Majorana's hypothesis becomes relevant for our understanding about neutrinos.

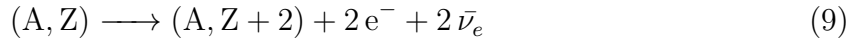
3.3 Neutrinoless double beta decay ($0\nu\beta\beta$)

The detection of neutrinoless double beta decays would have impact on our way of thinking about creation of matter in our universe. Since the lepton number conservation is violated by two units in this hypothetical decay, its discovery would change the assumptions of the Standard Model (where this number is conserved due to the masslessness of the neutrinos). If discovered, this process would be the first example for a nuclear reaction where only electrons are created. If this decay happens and only Standard Model assumptions are taken into account, it would confirm Majorana's hypothesis. Moreover, it could provide information on the absolute neutrino mass scale and ordering [14]. Briefly, when the neutrino mass scale will be established, one will know the lightest neutrino mass, which is m_1 in the case of normal neutrino mass ordering (NO) with $m_1 < m_2 < m_3$, or m_3 in the case of inverted neutrino mass ordering (IO) with $m_3 < m_1 < m_2$ [1].

The $0\nu\beta\beta$ decay mode can be mediated by several mechanisms, but the one requiring minimal changes in physics is the exchange of a light Majorana neutrino interacting via standard, left-handed V-A weak currents. The mass term which appears in the half life is the effective Majorana neutrino mass, which is the coherent sum of the neutrino parameters $m_{\beta\beta} = |\sum_i U_{ei}^2 \cdot m_i|$, where where U_{ei} are the elements of the neutrino mixing matrix, which include the Dirac and Majorana CP-phases, and m_i are the neutrino mass eigenvalues [14]. Certain rare isotopes are forbidden to decay via the beta decay. The mass of such isotopes is usually less than the daughter isotope after beta decay [1]

$$m(Z, A) < m(Z + 1, A) \quad (8)$$

These isotopes are energetically allowed, however, to decay via double beta decay, a nuclear process whereby the nuclear charge changes by 2 units while the atomic mass is left unchanged:



where two electrons and two electron antineutrinos are emitted.

In a neutrinoless double beta decay ($0\nu\beta\beta$) the following nuclear reaction would occur:



where two neutrons from the parent nucleus are converted into two protons and two electrons in the daughter nucleus without the emission of electron antineutrinos.

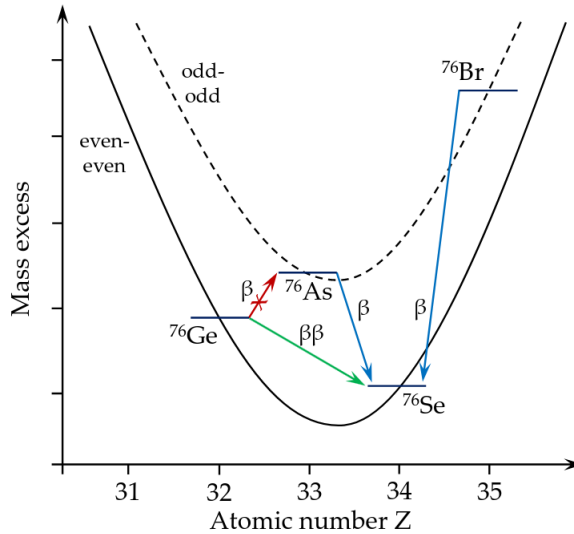
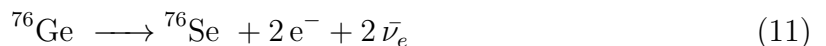


Figure 2: Mass parabola for isobars with mass number $A=76$ displaying possible and impossible decays from the studied ^{76}Ge isotope. While a beta decay to arsenic is forbidden, the double beta decay to selenium is possible for ^{76}Ge [17]

One can take the Weizsäcker's mass formula and deduce from the mass parabola displayed in figure 2 which isotopes are energetically eligible for a double beta decay. In order for an isotope to have this decay, a single beta transition would be forbidden. Of particular interest, ^{76}Ge is such an isotope, which can have the following double beta decay:



decaying into selenium and emitting two electrons and two electron antineutrinos.

The Feynman diagram for a neutrinoless double beta decay is shown in figure 3. In this diagram, it is shown that neutrinos are exchanged as virtual particles (through an yet unknown mechanism) and only two electrons are produced in the reaction. This diagram is drawn in the quark model of the neutrons, where the down quark changes to an up quark by emission of a virtual W^- boson. The Feynman diagram is not an actual picture of the decay kinematics, but a graphical representation of perturbative theory calculation for transition amplitudes in quantum mechanics.

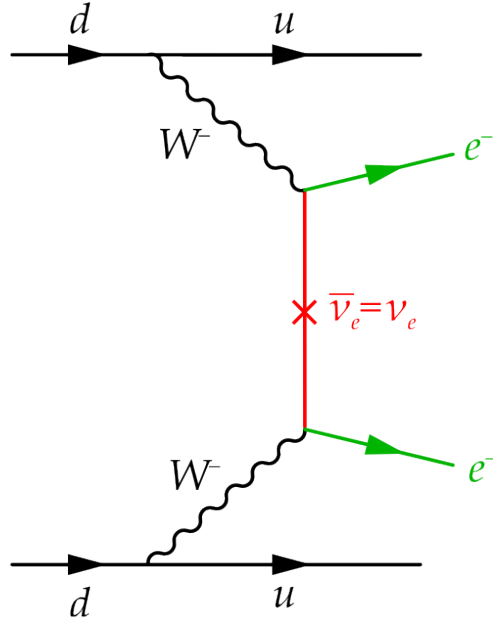


Figure 3: Feynman diagram for the neutrinoless double beta decay, displaying the exchange between the neutrino as a Majorana particle and the emission of two electrons [18]

Especially for the neutrinoless double beta decay, the transition elements are hard to calculate. If detected, this decay would be the slowest process ever observed with a half-life exceeding 10^{26} years [14]. This means that a nucleus will take on average more than a million billion times the age of the universe before undergoing a neutrinoless double beta decay [15]. To surpass this sensitivity, experiments must monitor thousands of moles of atoms for years, and have the capability to detect the neutrinoless double beta decay of a single one of them. Being a very difficult physical event to observe, the neutrinoless double beta decay also needs sensitive detectors with low background in order to be discovered. In the LEGEND experiment this mission is taken by high purity germanium detectors.

4 LEGEND experiment

The LEGEND experiment (Large Enriched Germanium Experiment for Neutrinoless Double Beta Decay) is a follow up experiment based on the legacy of MAJORANA DEMONSTRATOR and GERDA (GERmanium Detector Array). These experiments are well known for the great energy resolution, namely MAJORANA DEMONSTRATOR for the value of 2.53 ± 0.08 keV with respect to the full width at half maximum (FWHM) at $Q_{\beta\beta} = 2039$ keV (the kinetic energy released in the double beta decay) [6].

In LEGEND experimental proof of the neutrinoless double beta decay in ^{76}Ge is examined using high-purity germanium detectors made of material enriched in ^{76}Ge . The choice of the isotope is for precise reasons, namely because it is able to disintegrate via a double beta decay. Germanium is of paramount importance in ionizing radiation detection, because it is a solid crystal and also a direct semiconductor [17]. In addition, germanium has two important advantages over its competitor, silicon: a better medium energy to overcome the bandgap (2.9 eV against 3.9 eV [17]) and also a higher atomic number [19]. Therefore, germanium has a much larger linear attenuation coefficient (according to Bethe Bloch formula), which leads to a shorter mean free path for the interacting particles. Other important considerations for using germanium as a detector material for the $(0\nu\beta\beta)$ decay detection are: a high Q-value (since this gives a large phase space factor and the region of interest will be above the natural gamma background from other isotopes, like 2.6 MeV from ^{208}Tl), high natural abundance of the $2\beta\beta$ -isotope, an easy yet affordable enrichment procedure and last but not least a feasible detection technique dedicated to the studied isotope [28]. The most important factor is to operate the detector almost free of background. This is because sensitivity is a function of background and exposure. In case of an experiment without background, the discovery sensitivity would be described by a linear function of the exposure, while in a background-dominated regime the discovery sensitivity would scale with the square root of exposure [6]. Therefore, in LEGEND all objects that are placed in the set-up (ranging from the electronics to the wires and support rods) have to undergo screening, in order to have their background analysed.

While the detectors of LEGEND, as well as it was for the GERDA experiment, are placed underground in the National Laboratory of Gran Sasso, MAJORANA DEMONSTRATOR was operated in the United States - at Stanford Underground Research Facility (SURF) in Lead, South Dakota. The Gran Sasso mountains serve as a shield against muons and other particles of cosmic ray showers, which can produce background reactions in the detector.

The goal of LEGEND is to detect a peak at the end of the spectrum for electrons, in order to confirm the presence of the neutrinoless double beta decay in the studied germanium mass. This peak would originate from the exchange of neutrinos in the sought decay, while the electrons would gain therefore all energy, namely the whole kinetic energy released in the decay $Q_{\beta\beta} = 2039$ keV [6] (due to the non recoiling nucleus, which has a much higher mass and does therefore not further move). The signal peak for the neutrinoless double beta decay is shown in figure 4:

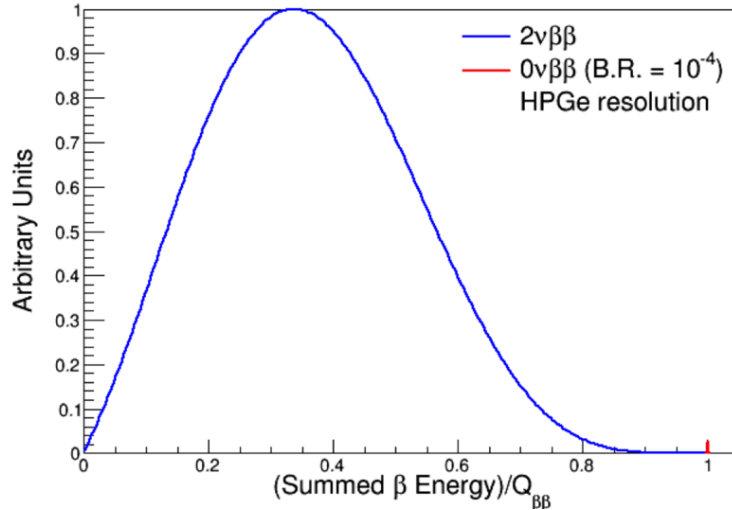


Figure 4: Normalized spectra for the two types of beta decays, where the neutrinoless case is displayed in red with a small peak at the end of the spectrum [19]

4.1 LEGEND-200

The name of the experiment phase originates from the target mass used for the detector, namely 200 kg of high purity germanium (HPGe- which contains around 90% ^{76}Ge) which are planned to be operated for five years. The targeted total exposure is $M \cdot t = 1 \text{ t} \cdot \text{yr}$ [6]. The experiment uses the location and technique of its predecessor GERDA in liquid argon, while bringing an upgrade to the set-up with the a better low-noise electronics system and more inverted-coaxial point-contact (ICPC) highly pure germanium detectors. An artistic view of the detector is shown in figure 5, where the detectors can be observed, surrounded by the liquid argon veto and the water tank:

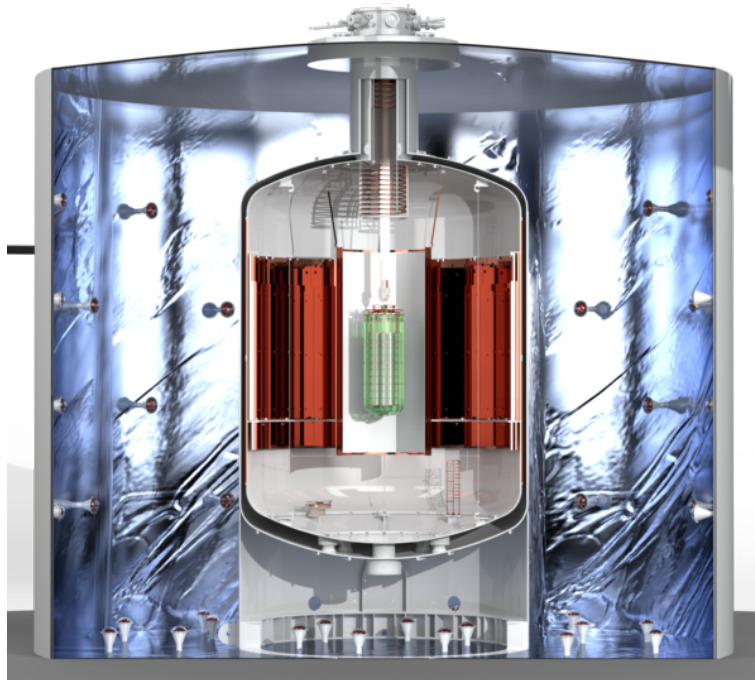


Figure 5: LEGEND-200 set-up with the germanium detectors enclosed in the green module, liquid argon veto system, cryostat and water tank [20]

Fundamentally, LEGEND makes use of liquid argon as an active veto for background interaction, but also as a passive shield against external radiation. Liquid argon serves at its normal operational temperature of 87 K also as a cooling medium for the germanium detector. Further, liquid argon also has the property of emitting scintillation light, when particles are passing through the medium and depositing energy in it. This scintillation light is read out by silicon photomultipliers and fibers. Scintillation light is useful in detecting background events, because it facilitates the recognition of simultaneous physical interactions happening outside of the detectors, like scattered γ rays [6]. In figure 5 one can also notice the cryostat where the argon is stored, surrounded by an additional larger water tank, which also acts as a passive shield for radiation and an active veto shield against charged particles like muons, which are detected via Cherenkov radiation [14]. This radiation is released when a charged particle passes through a medium with a speed greater than the speed of light in that specific medium. The medium becomes polarised and radiation in form of light is emitted. This light can be detected and the causing particle is distinguished by the shape of the light cone [1]. For a more detailed look at the individual detectors, figure 6 depicts the LEGEND-200 detectors at the mounting in a glove box (for protection against impurities):

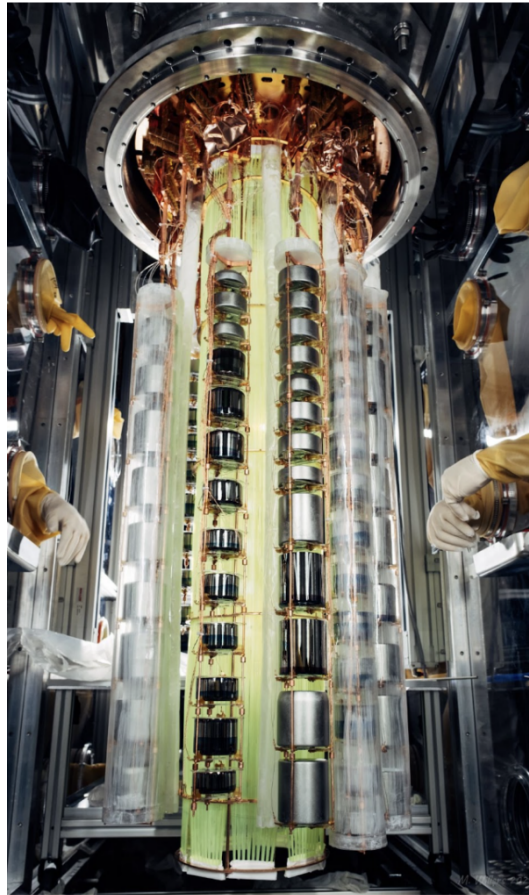


Figure 6: Closer look at the LEGEND-200 set-up in the glovebox, where one can observe that there are more detector types with different sizes supported by copper rods and connected by cables [21]

The assembly of detectors in LEGEND-200 is executed by using underground copper rods for mechanical support, while the electrical isolation is insured by plastic insulators. Below each detector there is a baseplate supporting a wire-bonded signal cable and an integrated circuit board to collect charges at the detector's p+ electrode [14]. In this experiment, the electrical elements are required to be electropure and almost background free. The idea is to implement the low-mass front-end (LMFE) electronics and the closure of the gain loop in the charge-sensitive amplifier (CSA) about a meter away, in order to set an upper limit on the bandwidth of signals and the rising edge—important for background event discrimination [14]. From the p+ electrode, which is bonded to the contact pad of the LMFE, a set of picocoaxial cables carry the amplified signals out of the cryostat and water tank to a data-acquisition (DAQ) system for waveform digitization and offline storage. A separate, high voltage picocoaxial cable wire-bonded to the detector's n+ electrode provides a high-voltage bias to deplete the germanium semiconductor detector [14].

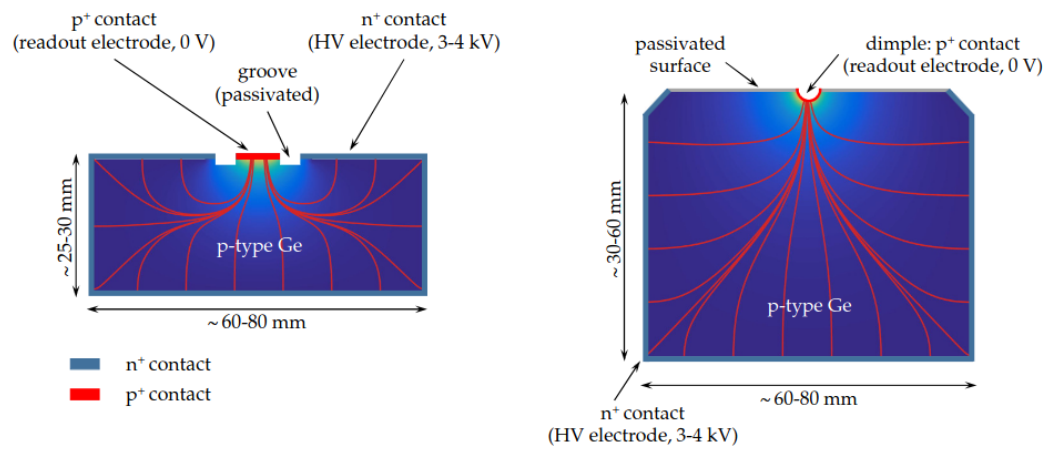
4.2 LEGEND-1000

By combining with the predecessor's LEGEND-200 ICPC detectors, approximately 400 individual ICPC detectors with an average mass of 2.6 kg will yield the huge total detector mass of 1000 kg. This will be the final phase of the project, aiming to obtain a total exposure of $M \cdot t = 10 \text{ t} \cdot \text{yr}$ and even less background, by using underground liquid argon as a veto for other particle events and better low-noise electronics [14]. Of particular significance are also the location of the experiment and reducing the signal read out of the electronics, by using a new technology. The applied specific integrated chip (ASIC) technology, would facilitate the integration of the entire charge sensitive amplifier (CSA) into a single low-mass chip while maintaining the spectral and noise performance achieved with conventional solutions [14]. In this last experiment phase, the discovery sensitivity is planned to cover the inverted-ordering neutrino mass scale. In addition, it will also probe the next order of magnitude for the normal ordering and other exchange mechanisms [14].

4.3 Detector types used in LEGEND-200

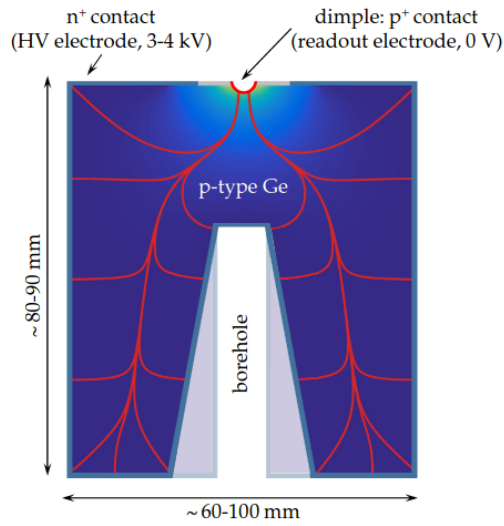
Several types of detectors were used in the experiment set-ups, all with the goal of improving sensitivity and background resolution. Some of them (BEGe, PPC, ICPC) will be discussed in the following subsections, with major differences lying in their geometry. The main advantage of these types of detectors is the enhanced capability of applying background rejection methods based on the shape of the signals (pulse shape) in comparison to the inverted coaxial cables used originally [14]. This is due to the specific geometry and arrangement of the electrodes leading to a strong weighting field close to the readout contact and to a relatively low field elsewhere. As a result, the signal shape of events that deposit their energy at a single location (single-site events, indicator for neutrinoless double beta decay signal events) in the detector is almost independent of the location of the energy deposition. This can be used to discriminate these events from those depositing their energy at multiple sites (multi-site events like Compton-scattered photons) or as an indicator for other background events, such as surface alpha and beta events [22]. There are several types of detectors used in LEGEND:

- BEGe: Broad energy germanium detectors have a cylindrical shape, but rather shorter length. They are less sensitive to surface backgrounds and have enhanced Pulse Shape Discrimination (PSD) capabilities which enables efficient background rejection [14]. The n+ electrode is represented by an infusion of lithium covering most of the surface, while the p+ electrode is represented by a small boron doped area located in the middle of the top flat face of the cylindrical slice and a circular non-conductive groove separating the two electrodes [25]. The p+ contact is located at the top surface separated from the n+ contact by an insulating groove, which is produced and covered by an insulating "passivation layer" made out of silicon or germanium oxide (depending on the producer). This passivation layer helps to keep steady-state currents (so-called "leakage currents") stable over time [25]. The Li-infused n+ surface presents a dead layer, which is insensitive. Although this dead layer is not sensitive to locate particle events, it can serve as a barrier for alpha particles, further reducing background.
- PPC: P-type point contact (PPC) germanium detectors are semiconductor detectors with a cylindrical shape, but greater height than BEGe's. While the n+ contact extends over the lateral and bottom detector surface, the p+ electrode (point contact) is formed by a small dimple located in the center of the top surface. The point contact size is significantly smaller compared to the one of typical traditional semi-coaxial detectors. Therefore, PPC detectors have a lower capacitance ($C_d \approx 1 - 2$ pF at full depletion) resulting in lower electronic noise, and thus in a better energy resolution. Moreover, PPC detectors can be operated at lower energy thresholds (< 1 keV) which makes them suitable for rare-event searches at small energies [22].
- ICPC: Inverted coaxial point cable detectors have the largest size of all three detector types, typically having a cylindrical shape. The increased size and mass comes with the motivation to improve energy resolution and background and also reach a smaller capacity. As a difference, it exhibits a concentric borehole in order to refrain from undepleted regions together with optimized electric fields in the inside. Their creation goal consists in having an increased mass for better signal sensitivity, since BEGe and PPC detector sizes could not be further extended, due to the increase in undepleted material regions. On one hand, these ICPC detectors possess low capacitance, low threshold and good background rejection performance, but on the other hand the extended size increases drift times to values around $\tau_{drift} \approx 2\mu s$ where collective effects like diffusion and self-repulsion of the charge cloud have to be taken into account [22]. The p+ contact is located at the top surface separated from the n+ contact by an insulating groove. ICPC detectors also present the passivation layer. This provides for them, as well as for the other detector types further protection from humidity or conditions which favour deterioration.



a) Broad energy germanium (BEGe) detector

b) P-type point contact (PPC) detector



c) Inverted coaxial point contact (ICPC) detector

Figure 7: Detector types used in LEGEND with the BEGe, PPC and ICPC types [22]

5 Experimental techniques

5.1 Semiconductor detectors

Semiconductor detectors provide a fine energy resolution, being an instrument of significant advantage in experiments for rare event searches [6], like the detection of the hypothetical neutrinoless double beta decay sought in LEGEND. In rare event search detectors need a strong sensitivity to discriminate the event from background. The improved energy resolution over the gas detectors originates in the better statistics regarding the number of signal carriers (charges) excited by a radiation interaction. Germanium is a semiconductor with strong properties for radiation detection. On average, 3 to 5 eV are needed to produce an electron-hole pair in a semiconductor[17]. In order to understand why germanium is a semiconductor, one needs to look at its bandgap structure.

5.1.1 Bandgap structure

As in atoms, the energy of electrons in solids is confined to particular energetic states called energy bands. The band gap represents the difference in energy between the valence band of electrons and the conduction band. The valence band is the highest energy filled band, and is completely filled in a semiconducting material [29]. The conduction band represents the energy states of electrons, which are able to dissociate from a particular atom and become free charge carriers in the material. The conduction band electrons are the most energetical electrons in the material, and are loosely bound, not limited to any particular lattice site. The electrons from the valence band are less energetical and are bound to particular lattice sites. The factor which decides if the material is a semiconductor, metal or insulator, is the size of the band gap. In comparison to insulators, semiconductors exhibit a relatively small gap between the conduction and valence band, while in metals one would encounter an overlap of the two bands.

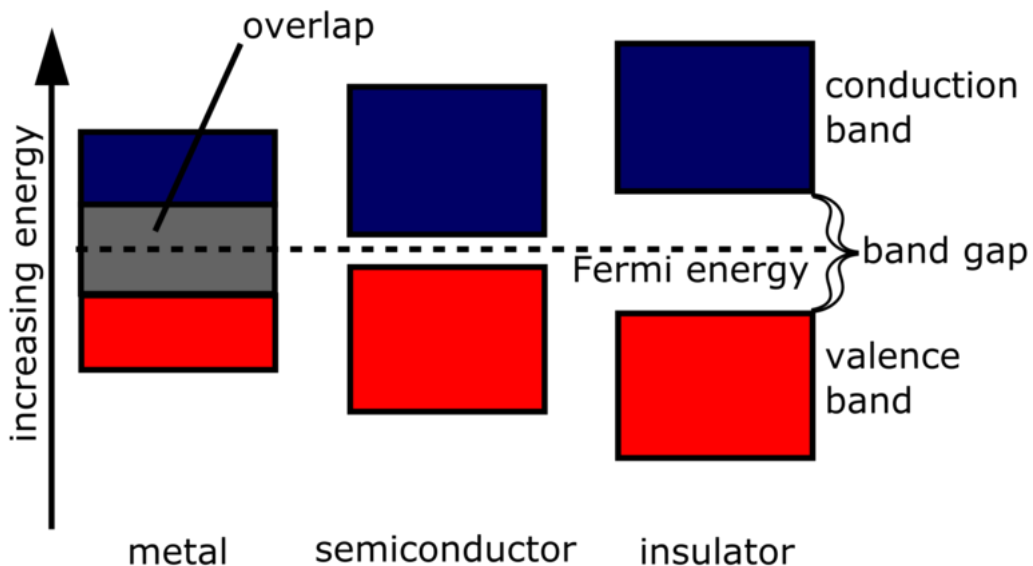


Figure 8: Comparison between band gaps of metals, semiconductors and insulators with valence and conduction band displayed [23]

Semiconductors have some conductivity in contrast to insulators, because electrons can overcome the band gap by thermal excitation [33]. While electrons in insulators can not jump the the band gap via thermal excitation, the electrons from metals can move freely between the conduction and valence bands. This band gap can be also be surpassed by an electron, if a physical scattering process happens and gamma quanta deposit energy in the valence band. The probability of overcoming the band gap by thermal excitation happens with a probability described by the Boltzmann distribution [29]:

$$P(T) \propto T^{3/2} \exp^{-\frac{E_g}{2kT}} \quad (12)$$

where k is Boltzmann's constant, E_g the bandgap energy and T the temperature. This formula displays also one very important operational feature of germanium as a material for semiconductor detectors. Germanium detectors must be operated at low temperatures, of under 100K (77K in liquid nitrogen and 87K in liquid argon [29]) in order to avoid thermal excitation, since the probability to surpass the bandgap is an exponential function of the temperature. At room temperatures, electrons would easily overcome the bandgap and produce a so called leakage current, which is indeed a source of noise. Too high levels of leakage current are making the detector inoperable. Electrical noise is defined as a disturbance of the signal that hinders the ability to distinguish between signal structures. Therefore, the electrical noise reduces the resolution and performance of the detector.

5.1.2 Doping

In an idealized model a perfect semi-conductor would have no conductivity at absolute zero temperature. In reality imperfection creates the conductivity: because small residual impurities always remain present in the crystal structure and affect the band levels and band gap. By calling impurities "acceptors", one means that an acceptor possesses more holes (positive charge, therefore called p-type), while "donor" impurities bring more negative charge (electrons, the n-type) [17]. The most widespread examples are: crystals doped with boron for p type and crystals doped with phosphorous for the n-type semi-conductor [19].

Scientists often choose to enhance properties of the materials by intentional introduction of impurities into the lattice, called doping. By bringing n-doped and p-doped material together, one creates a diode junction (often called p-n junction) [17]. Although the positive and negative charges are brought together, p-n junction consists of mostly electrically neutral atoms, while some of them are missing electrons or holes.

Some of the unpaired electrons of the donor impurities in the n-type material diffuse and advance across the junction into the p-type material to recombine with the holes. The donor impurities that those electrons came from are no longer electrically neutral – they now have a positive charge. Similarly, holes from some of the acceptor impurities in the p-type material "diffuse" across the junction to combine with donor electrons on the n-type side of the junction. This leaves those acceptor impurities with a negative charge [17].

By bringing electrons and holes near the junction together, one produces a non-conductive region almost completely lacking free charge carriers, called the depletion region. It serves as the active volume of the detector [29]. There is a positive charge associated with the n-type material side of the depletion region and a negative charge in the p-type material side of the depletion region. This creates a “natural” electric potential across the depletion region. This potential has to satisfy the Laplace equation $\nabla^2\phi = 0$ Because of the electric potential, an electric field is formed, described by the following equation:

$$\vec{E} = -\vec{\nabla}\phi \quad (13)$$

Applying a “reverse bias” voltage increases the size of the depletion region. This means that the electrical contact on the n-type material is given a positive potential (anode) with respect to the potential on the p-type material (cathode). One can picture this by imagining a pull of the holes and electrons associated with the impurities closer to the cathode and anode respectively - this increases the width of the depletion region [29].

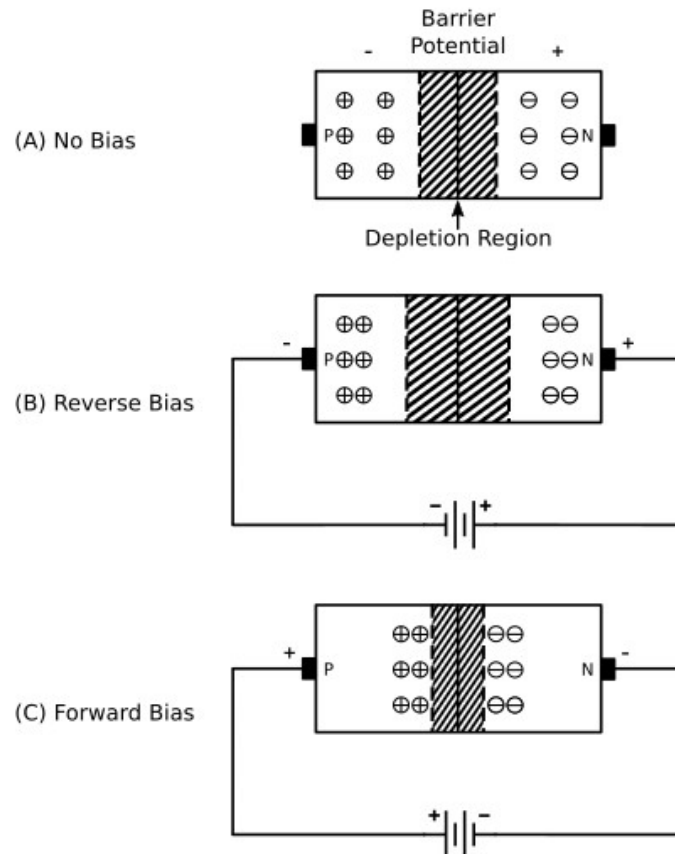


Figure 9: Comparison of the increase of depletion region by applying a voltage in reverse bias and decrease of depletion region in forward bias regime [24]

5.1.3 Working principle of semiconductor detectors

The working principle of semiconductor detectors can be described through the following steps, being a solid state analogy to ionization chambers:

- The ionizing radiation penetrates the sensitive volume of the detector and interacts with the semiconductor material through physical processes. The types of interaction between gamma radiation and matter are: the photoelectric effect, Compton scattering and pair production, depending on the energy of the gamma quanta [29].
- The result of this radiation interaction is the ionization of the atoms in the semiconductor and the producing of electron-hole pairs. As a result, many electrons are transferred from the valence band to the conduction band, and an equal number of holes is created in the valence band. The number of electron-hole pairs is proportional to the energy of the radiation to the semiconductor [17].
- However, the created electrons and holes need external help to move at the reading surface of the detector. Possessing opposite signs of electric charge, the electron-hole pairs would normally just randomly diffuse in the medium, trapping on crystal defects or mutually attracting and recombining immediately [17]. By applying an electric field, electrons and holes travel in opposite directions to the electrodes (the electrons move to the cathode and holes to the anode, because of having opposite charges), where they result in an electric pulse that can be measured in an outer circuit. As the charge drifts through the detector, it also induces a charge at the point contact according the the Shockley-Ramo theorem [29]:

$$I_{readout} = - \int \vec{\nabla} \phi_{weighting} \cdot v_{drift}(t_0) dq \quad (14)$$

which states that the instantaneous current is given by the product of the charge, the instantaneous velocity (which may depend on the electric field) and the value of the weighting field at the position of the charge. Then, pulses are amplified through the electronics system, in order to be read out on the digital apparatus. The details about electronics will be discussed in section 5.2.

5.2 Electronics and charge sensitive amplifier

In figure 10, one can see the electrical scheme of the set-up. The role of the high voltage filter (effectively an RC loop) is to reduce the noise, by suppressing high-frequency noise potentially introduced by the bias voltage supply. Then, the so called front end electronics and the preamplifier constitute the charge sensitive amplifier.

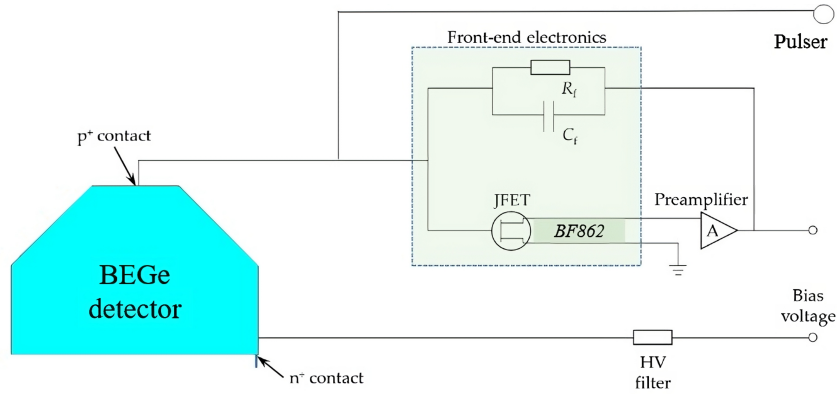


Figure 10: Schematic of the set-up and its electronic components, displaying the shape of the BEGe detector, as well as the components of the charge sensitive amplifier, JFET BF862 and pulser. Adapted from [21]

The charge sensitive amplifier (CSA) consists of an operational inverting voltage amplifier or other high gain semiconductor circuit with a high input resistance and feedback capacitance. This device integrates a current signal and generates a voltage signal with an amplitude proportional to the incoming input charge. The purpose of the feedback resistance is to discharge the feedback capacitance. Further, the resistance provides stability to the circuit, a lower frequency limit on the amplifier and also sets the gain at a specific value, so that the input offset voltage will practically have no impact on the output offset voltage [33]. For simplicity, the effect of the junction gate field effect transistor (JFET) can be neglected, as the ideal operational amplifier has a time independent gain.

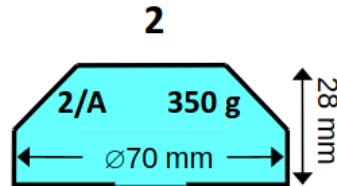


Figure 11: Geometrical shape of the BEGe detector module used for measurements at the Technical University of Munich. Adapted from [25]

The detector used has the shape sketched in the figure 11, being a BEGe type. The Li-infused n+ electrode is covering most of the surface, while a boron implanted small-area p+ electrode is located in the middle of the bottom flat face of the cylindrical slice and a circular non-conductive groove is separating the two electrodes.

6 Test of different high voltage contacts

Germanium detectors from LEGEND operate with low-noise electronics for the charge amplification in order to have their signals read out without inducing more background. One needs to understand the electrical scheme to have an overview of the detector and how the components can influence each other. As in figure 10, the set up is divided in the high voltage power supply, a high voltage filter, the detector and the charge sensitive amplifier. In addition, a pulser is added to study the response of the electronics. As a technical note, the pulser injects the signal separated from the detector configuration directly to the CSA. The pulser output represents a square topped pulse, that is given to the preamplifier via a separate input. The use of the pulser is important in gamma radiation detection, since it can monitor the stability of the electronics systems with time [22].

The functional electrical scheme in figure 12 follows this principle: After high voltage (a few thousand volts) is applied to the detector, the high voltage filter blocks the produced high-frequency noise. This low-pass filter is made out of a resistance and a capacitance (effectively an RC loop with a resistance in magnitude of a few $G\Omega$ and a small capacity of a few nF). When the so-called reverse bias voltage is applied to the detector, one will choose the voltage value for a full depletion. Following this, the detector becomes operable and acts in the electrical scheme as a capacitance of magnitude in the order of a few pF . After electron-hole pairs are created, the charge collected on the electrode is integrated by the CSA, sending the output voltage to the data acquisition system.

In this thesis, the idea to test the relationship between the high voltage contacts and the performance of the detector originates from the performance problems of detectors in LEGEND. Because several problems have been encountered in calibration runs at LEGEND, a hypothesis was formulated and the test of the high voltage contacts became relevant [30]. These problems and the formulated solution hypothesis will be addressed in the next subsection.

6.1 Observed issues and possible explanation

In LEGEND-200 the cryostat hosts ten strings with detectors [14]. However, during calibration runs it was observed, that not all detectors were registering coherent results. In some calibration runs, several problems have been encountered in some of the LEGEND-200 inverted coaxial high-purity germanium detectors. [32] These issues are related to the performance of the detector and the gains of the pulser. Aspects that are included under the term performance are: the energy resolution, the shape of the pulses detected and also the active volume of the detector.

In LEGEND-200 several of the ICPC detectors show drifting gains during calibration runs in liquid argon, even though they perform well in vacuum. The observed effects are the upward shift of the 2615 keV peak, while the pulser peak experiences a downward shift. Furthermore, the pulser peak drift is smaller than the 2615 keV drift [32].

These results were the premise of executing voltage scans of those imperfect detectors, then of the entire array. The scan represents an operation of the detectors at different high voltages in steps of a few hundred volts, until the operational voltage is reached.

The goal was to determine how the detector capacitance affects the observed shifts. One would be also interested to see if the depletion voltage measured in the vacuum cryostat is the same as the one in liquid argon.

The hypothesis about the performance problems starts by regarding the high voltage contact on the detector as the cause. Particularly, if the high voltage contact exhibits a non-ohmic behaviour, new effects can affect the detector performance, i.g the energy resolution, which will be described in the following. The non-ohmic behaviour means that the contact possesses a high resistance and also a stray capacitance. It manifests itself through a variable resistance, that changes in a way which depends on the voltage passing through it. The stray capacitance is a completely parasitic capacitance, which forms due to the proximity of electrical elements in a circuit. In electrically charged surfaces which are too close to each other, an electric field and a capacity are created. Therefore, when wires are mounted too close to each other, they can produce a stray capacitance, which affects the current flow in the circuit. This capacitance can serve to impede or block low-frequency signals (because of having high impedance to low-frequency signals). Thus, it is difficult for low-frequency signals to pass through a circuit that exhibits capacitive qualities [33].

In the case of a connected and well functioning high voltage contact, as in the scheme drawn in figure 12, electrons are collected to the n+ (Li) contact, which is opposite and almost equal to the main point-contact signal. This signal from the lithium contact could couple through the detector capacitance to the point contact. However, in this ideal case, because there is no resistance or capacitance to the high voltage filter, the signal disappears into the high voltage filter capacitance.

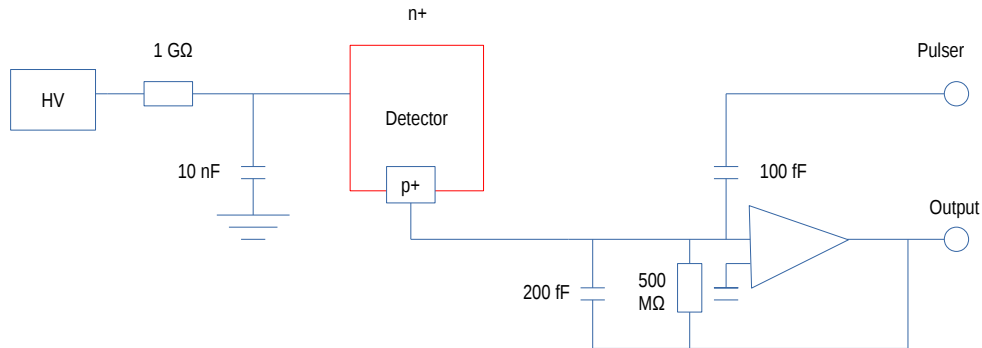


Figure 12: Schematic of the ideal case, where the detector is completely functional and no bad contact is formed. Here the components are the high voltage filter, then the detector and the CSA with output channel and pulser

In the case of a bad contact (high resistance and stray capacitance), shown in figure 13, the charges collected on the lithium n-contact, are forced to couple to the p-contact. The n+ signal is opposite the p+ signal. In the hypothesized situation, the n+ (negative) signal partly couples to the p+, therefore partly canceling the (positive) signal there. That coupling decreases as the detector capacitance decreases, so the apparent gain for the p+ signal increases.

One has to bear in mind that argon is a noble gas, where ionization electrons and scintillation light is produced when charged particles pass through this medium and store energy in it [23]. The effect induced by the argon medium would be the creation of electrical charges, which migrate and stay in the passivated surface of the detector. These excess electrons change the electric field and the surface density of electrons adjusted to reproduce the increase in the depletion voltage. This happens as long as the detector is not fully depleted and therefore, a change of the detector's capacity also occurs. As long as the detector is not fully depleted, the detector capacitance depends on the high voltage contact (or charges in liquid argon and collected on the passivated surface), which causes the drift observed in the gain of the pulser.

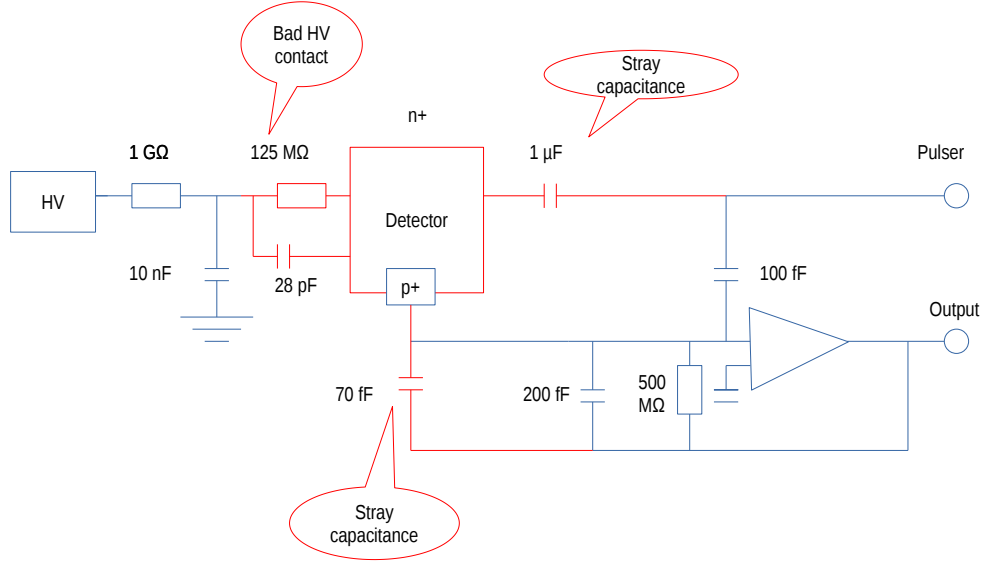


Figure 13: Schematic of hypothetical case, where the contact is not ideal and presents additionally a resistance and a capacitance as a RC loop. Further, stray capacitances in the vicinity of the detector arise due to the proximity to the other connections in the circuit. The bad contact and the stray capacitances are drawn in red.

In order to extract charge carriers from a semiconductor detector without facing a significant potential barrier (manifested in Schottky contacts), one would need to create ohmic contacts at the interface of bonding [29]. The ohmic contact behaviour brings to the contact between a metal and a semiconductor an allowance for carriers to flow in and out of the semiconductor, having no direct impact on electrical performance of the semiconductor material and detector. On the other hand, a bad contact would create a high resistance and also a capacity, behaving therefore like a RC loop. In the case of this thesis, the contacts were intentionally mounted with a poor quality. The question addressed in this study is the impact of a bad high voltage contact on the performance of the detector. This test was done in order to directly see what implication the high voltage contact can exhibit on the detector.

6.2 Experimental setup

Three types of contacts have been mounted for the n type contact onto the a non-enriched natural germanium BEGe detector, similar to the ICPC used in LEGEND:

- signal (p+ contact)
- aluminium (n+ contact)- the ideal LEGEND case
- raw lithium (n+ contact)- for comparison with aluminium
- polished lithium (n+ contact)- worst case

and test the non-enriched natural germanium detector implanted with boron doping in liquid nitrogen at 77K. One has to remember, that natural germanium (a mixture of its isotopes) is used in this test and not the enriched ^{76}Ge as in LEGEND. The detector used is produced with the same procedure as BEGe detectors in GERDA and LEGEND. Due to mechanical problems in LEGEND, some bonds were not be performed to the aluminium plate, but to the polished lithium plate. Regarding the contacts, aluminium is the same material used in the test of the LEGEND-200 experiment, while lithium was chosen simply for comparison with a different element. However, the idea to build also a polished lithium contact has the motivation to compare the type of the surface, since the raw lithium presents a rather rough facet. The wires used for the contacts were made from aluminium. Figure 14 displays the mount of the contacts on the detector:

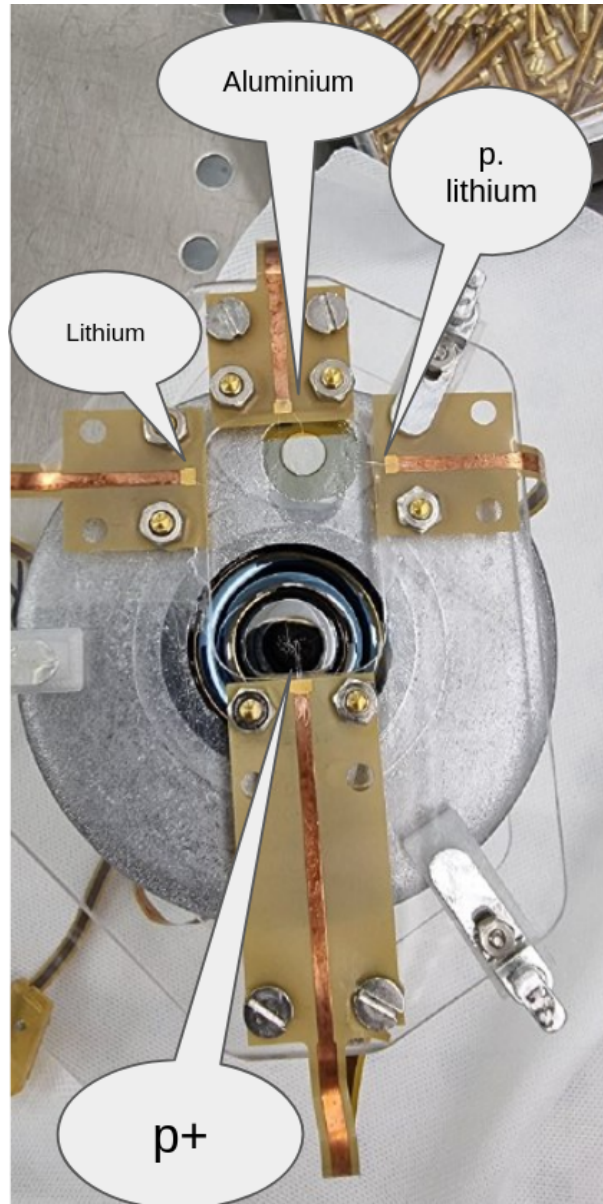


Figure 14: Mount of contacts on the germanium detector done in the laboratory, with the signal contact marked as $p+$ on the bottom side and the three studied contacts on the top side.

A further picture shows the detector mounted in the glovebox, in figure 15. The glovebox has the role to protect from the humidity condensing that arises when the detector is lifted from the liquid nitrogen. Therefore, low levels of oxygen had to be kept in the glovebox for the tests with the detector. In other experiments gloveboxes are used as a protection for the set-up from air particles, radon contamination and human impurities.

The laboratory procedure of the measurement during the calibration employed the protocol described below: The bonds were performed on the detector and the set-up was sunk in liquid nitrogen by using a mechanical support system. The CSA was also sunk in liquid nitrogen. Then, only on one contact at the time, high voltage was applied until the detector was fully depleted. On the oscilloscopes waveforms were verified to have a good shape and represent physical events. If they passed the test, the thorium source

was placed outside, on the shell of the cryostat for the calibration. In the end, the measurement was performed for several hours in order to collect enough statistics for the analysis. The data was collected with a FlashCam device and converted to digital hdf5 data format for the computer.

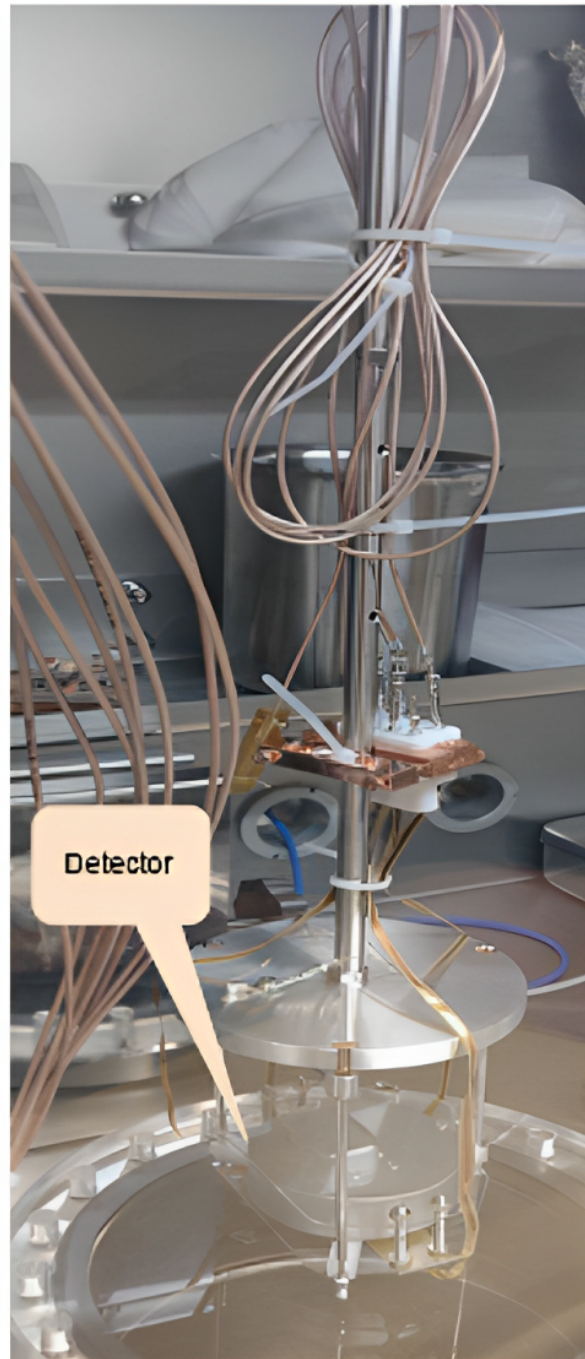


Figure 15: Detector in glove box with support system and connection wires to the high voltage. The detector is at the bottom of the picture, under the glass window sunk in a liquid nitrogen dewar

7 Resistance measurements on the contacts

One important run of measurements aimed to determine the resistance between the electrical contacts. This was done once with the detector mounted in the glovebox at room temperature and once with the detector cooled down and immersed in liquid nitrogen, but without the charge sensitive amplifier. By using a multimeter, the probes were put in the gate corresponding to each type of contact and then the direction was reversed (the plus contact went to minus and vice versa) in order to check if there exists a diode behaviour.

In another measurement run, a test was done to see how the contacts are actually working and behaving, by trying to plot their I-V (current-voltage) curves. Once again, the germanium detector was cooled in nitrogen at 77K. The goal was to measure the current with a picoammeter at fixed voltage values in steps of one volt (for instance from -16 to 16 volt). One would expect to see a diode behaviour between the n and p contact, described by the following diode equation of Shockley [34]:

$$I_D = I_S(e^{\frac{qV_D}{kT}}) \quad (15)$$

where I_D is the diode current, I_S is the reverse-bias saturation current, while k represents Boltzmann's constant and T the temperature. This equation describes a real diode, with a potential barrier (0.3 V for germanium) and a forward resistance. In contrast, the ideal diode behaves completely like a switch, closed on forward bias and open on reverse bias. The expected behaviour of a semiconductor at absolute zero temperature is that it becomes a perfect insulator. In our case, we expect a much higher value of the resistance. This happens, since at low temperatures, electrons have less energy to escape from the conduction band and move freely through the crystal lattice.

The results are presented in the next tables, where one can remark how big the resistance became when the detector was cooled down at 77K, namely increasing by several orders of magnitude. Therefore, these contacts can be regarded as "bad" ones, inhibiting a perfect flow of the current to the detector. The abbreviation "p. lithium" stands for polished lithium.

	Signal (-) [Ω]	Lithium (-) [Ω]	Aluminium (-) [Ω]	p. Lithium (-) [Ω]
Signal (+)	-	210	55	50.000
Lithium (+)	180	-	170	48.000
Aluminium (+)	55	200	-	48.000
p. lithium (+)	7800	8000	7700	-

Table 1: First measurement of the resistance between contacts on the germanium detector (measured at room temperature 22 °C). This time, the measurement was performed between the plus and minus contacts, as indicated by the brackets

	Signal (+) [Ω]	Lithium (+)[Ω]	Aluminium (+)[Ω]	p. lithium (+) [Ω]
Signal (-)	-	200	54	7700
Lithium (-)	210	-	210	7800
Aluminium (-)	55	170	-	7700
p. lithium (-)	48.000	48.000	49.000	-

Table 2: Second measurement of the resistance between contacts on the germanium detector (measured at room temperature 22 °C). This time, the measurement was performed between the plus and minus contacts in a reversed way, as indicated by the brackets

	Signal (-)	Lithium (-)	Aluminium (-)	p. lithium (-)
Signal (+)	-	263 Ω	1.8 M Ω	infinity
Lithium (+)	261 Ω	-	1.8 M Ω	infinity
Aluminium (+)	212 k Ω	212 k Ω	-	infinity
p. lithium (+)	328 k Ω	328 k Ω	2.3 M Ω	-

Table 3: First measurement of the resistance between contacts on the germanium detector (measured at room temperature 77 K). This time, the measurement was performed between the plus and minus contacts as indicated by the brackets. In the table, infinity means that the resistance was too high to be read out, so no good contact could have been formed in that direction.

	Signal (+)	Lithium (+)	Aluminium (+)	p. lithium (+)
Signal (-)	-	183 Ω	210 k Ω	328 k Ω
Lithium (-)	262 Ω	-	210 k Ω	328 k Ω
Aluminium (-)	2 M Ω	2 M Ω	-	2.4 M Ω
p. lithium (-)	infinity	infinity	infinity	-

Table 4: Second resistance measurement between contacts on the germanium detector, in liquid nitrogen at 77 K. The bracketed sign indicates the resistance with the positions of the contacts switched in the reversed way, where infinity represent a non measurable resistance and therefore no contact

As a first conclusion, all n-p contacts exhibit the behaviour of a real diode in figures 16 to 18, but all with a different exponential rise time. The difference in exponential rise is caused by the electrical resistance formed in the contact. The following hierarchy is observed: polished lithium has the highest resistance, followed by aluminium and raw lithium. With a resistivity of $\rho_{Li} = 9.28 \cdot 10^{-8} \Omega m$ for lithium and $\rho_{Al} = 2.82 \cdot 10^{-8} \Omega m$ for aluminium and $\rho_{Ge} = 4.6 \cdot 10^{-1} \Omega m$ for germanium [34], the result of the measurement at room temperature is understandable, since it reflects the hierarchy of the resistivity, on which it depends linearly as stated in equation 16. At $T = 80K$ lithium has a resistivity of $1 \cdot 10^{-8} \Omega m$ and $2.45 \cdot 10^{-9} \Omega m$ for aluminium, while germanium has a resistivity of $4.88 \cdot 10^{-4} \Omega m$ [35]. The resistance of a wire is directly proportional to the resistivity after this equation [33]:

$$R = \rho \cdot \frac{l}{A} \quad (16)$$

where R stands for resistance, l for length, A for surface of the wire and ρ for resistivity of the material. Resistivity depends itself on the charge and hole mobility of the semiconductor [33]. It was studied in the reference [16], that the resistivity of pure germanium is influenced by additional factors besides temperature, such as doping, impurity concentration and contamination with gas. Therefore, the discussion about the resistivity is useful to understand that at low temperatures, the behaviour of germanium is opposite to that of metallic ones, creating higher resistances in contacts.

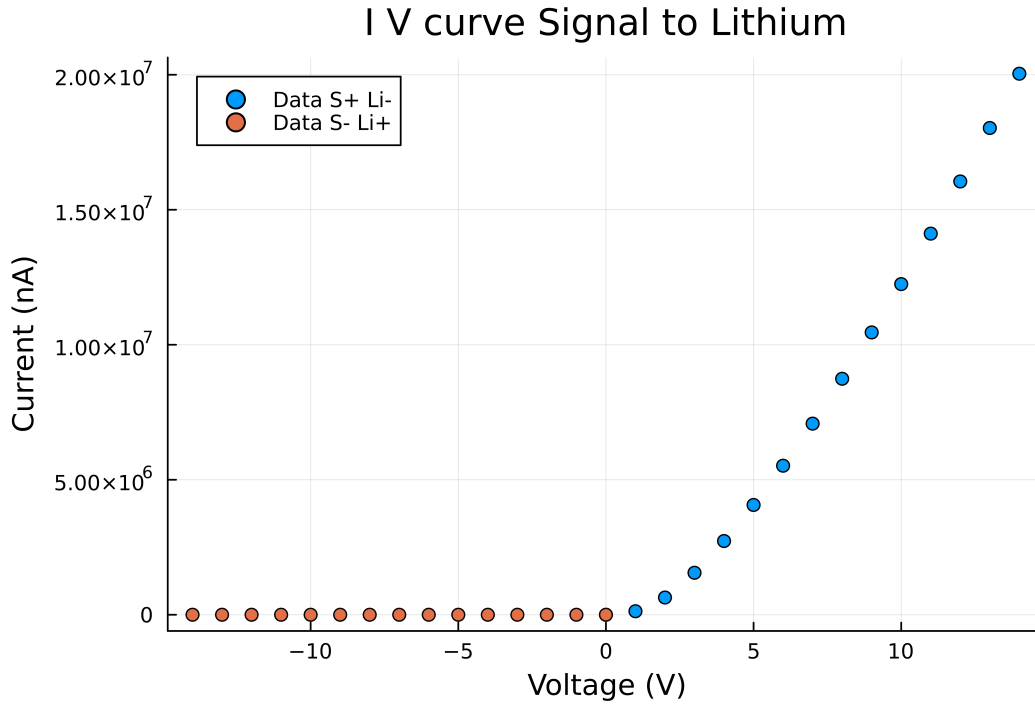


Figure 16: I-V curve for signal lithium contact

The I-V curve (standing for current-voltage) for the signal-lithium contact in figure 16 represents an exponential rise when the positive contact is mounted in the signal channel and the negative one in aluminium. In the reversed sense (S- Al+) only an insignificant quantity of current can pass through, thus confirming the specific diode blockage in this direction. Further, at small positive voltages (between 1 and 5 V) one can observe an approximately linear behaviour of the resistance, better displayed in the comparison done in figure 19.

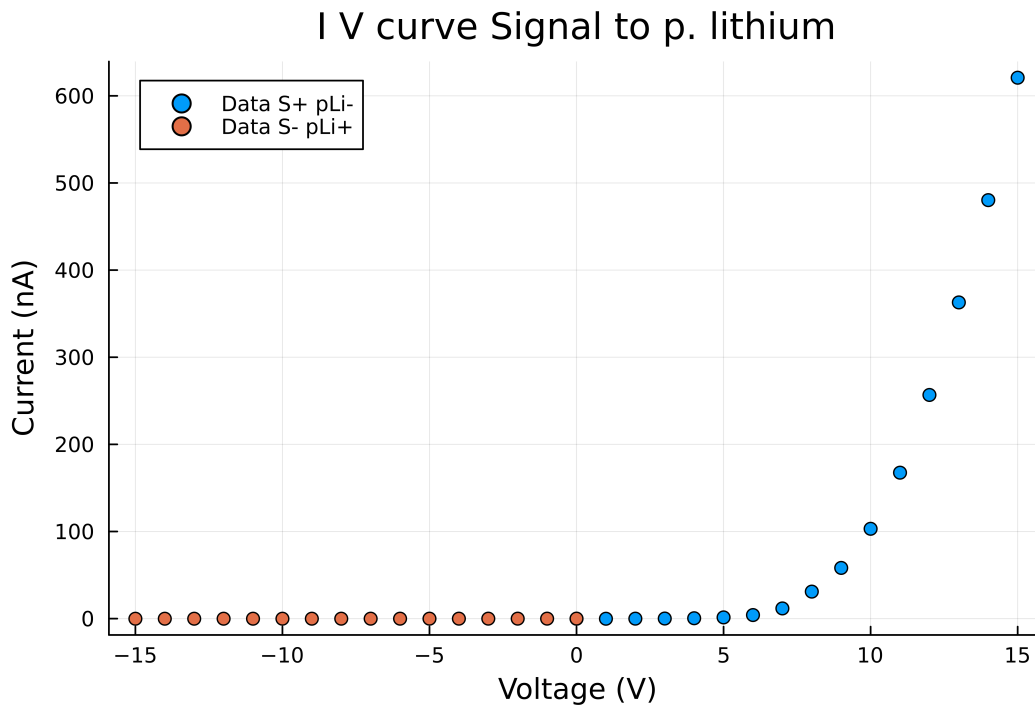


Figure 17: I-V curve for signal polished lithium contact

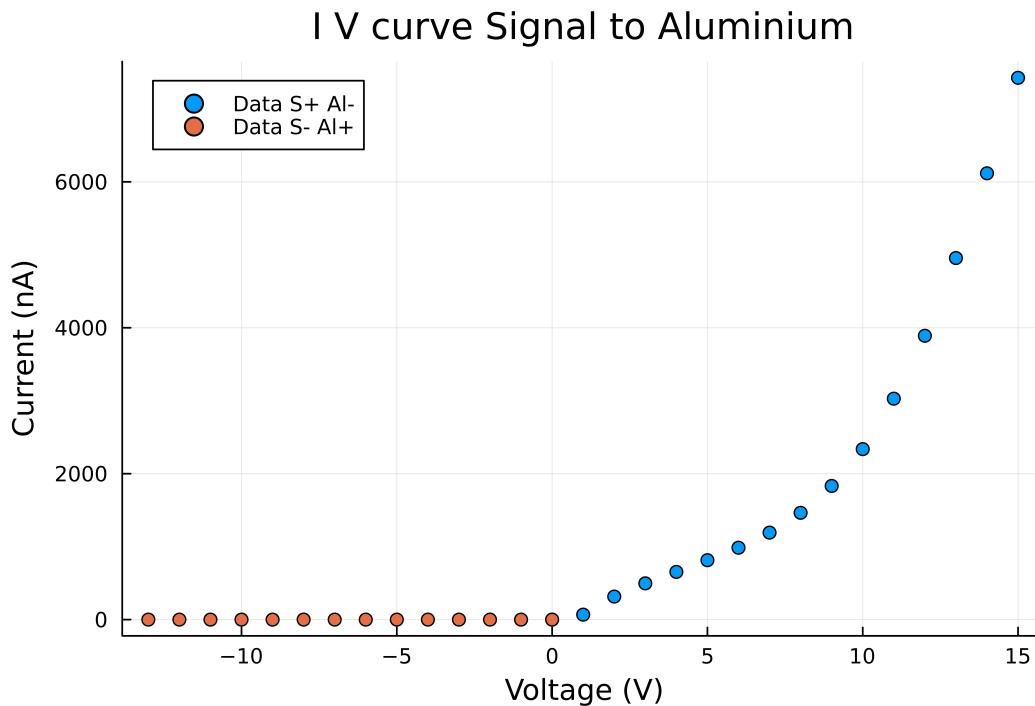


Figure 18: I-V curve for signal lithium contact

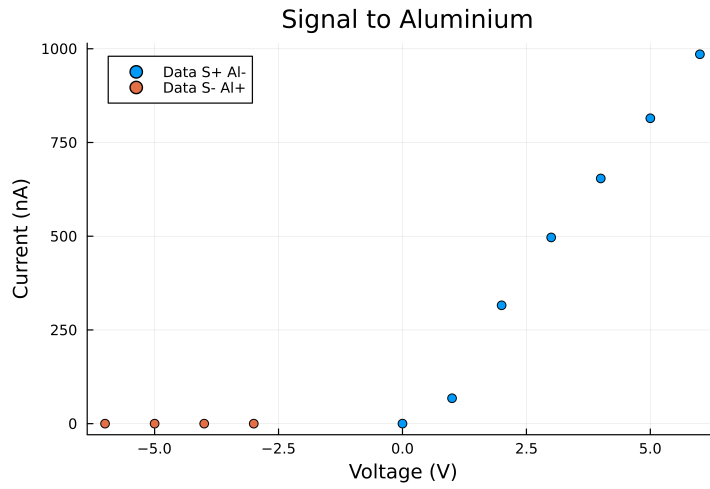
The I-V curve for the signal-polished lithium contact in figure 17 also displays the characteristic exponential rise in one direction and current blockage in the other, thus confirming a diode behaviour.

The I-V curve for the signal aluminium contact in figure 18 also displays a fast exponential rise in the operating direction, yet also current blockage in the reversed direction.

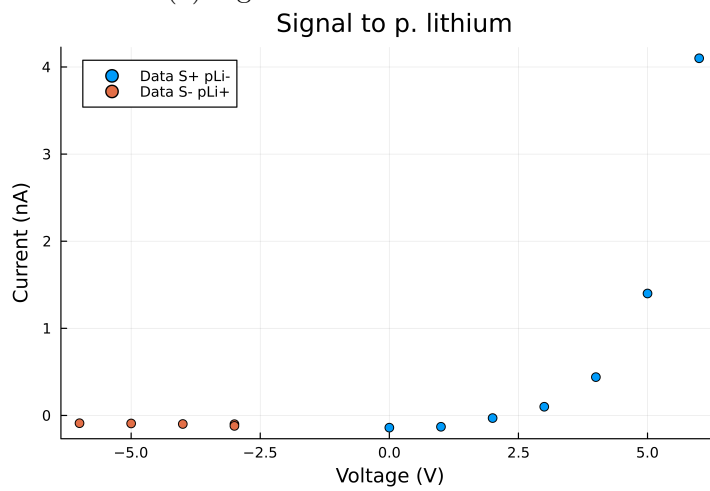
This also confirms the diode behaviour, but with a much higher resistance on the contact.

The highest currents are measured in the lithium contact, followed by the aluminium, with polished lithium being the last one. This curve behaviour confirms the measurement of the resistances and the predicted order, because the polished lithium contact had the biggest resistance, followed by aluminium and raw lithium. Therefore, one would expect to see in the spectroscopy analysis a worsening of the detector performance or spectrum shape in the contact with high resistance in comparison to the others, namely the polished lithium.

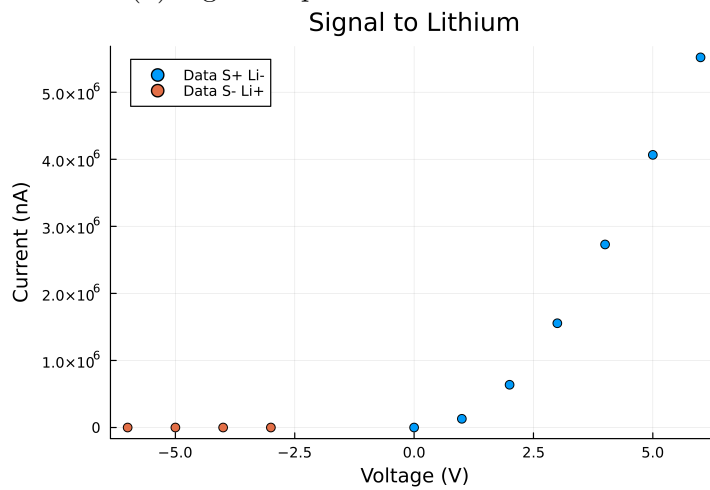
Further, more detailed figures were made for the contacts, where only the current values corresponding to voltages between -6V and $+6\text{V}$ were plotted. On these plots in figure 19, one can see that the aluminium contact has in a good approximation a constant rise until 6V . The rise of aluminium is faster than the one for polished lithium, where the I-V curve is convex and not straight in the studied interval. The curve for lithium can be regarded as linear only in an approximation between 2V and 6V . The convex shape shows that the contact is not ohmic and Ohm's law is not a good approximation for calculating the resistance, suggesting a poor quality of the polished lithium contact in comparison to the lithium and aluminium contacts.



(a) Signal to aluminium contact



(b) Signal to polished lithium contact



(c) Signal to lithium contact

Figure 19: Detailed plot of the I-V curves for the contacts between the voltages of -6V and +6V, displaying the features of the rise more clearly

8 Spectroscopy analysis

A radioactive ^{228}Th sample was placed on the cryostat vessel, which enclosed the germanium detector. This serves as a calibration test of the detector operated in liquid nitrogen at 77K. The radioactive isotope ^{228}Th (half life $T_{1/2} = 1.9$ yr) is unstable and disintegrates through several alpha and beta decays to the stable nucleus ^{208}Pb . The decay chain is displayed in figure 20. Some excited states produced in the decay chain return to the ground state by emitting gamma radiation. Most of the gamma rays are emitted after the decays of ^{212}Bi and ^{208}Tl . The advantages of this calibration source are the following: the intense peak lines in the spectrum, long enough half life and prominent full energy peak at 2614.5 keV, around the zone of interest in LEGEND for the detection of the neutrinoless double beta decay, namely $Q_{\beta\beta} = 2039$ keV [23].

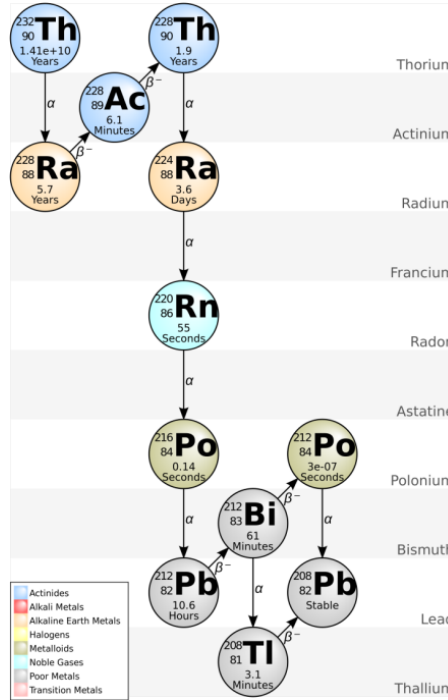


Figure 20: Decay chain of thorium [26]

8.1 Analysis of waveforms

The analysis of waveforms is of paramount importance in experiments, where high sensitivity is needed, such as LEGEND or GERDA, because it is used as a distinction between events and background. The detector response was analysed employing software written using the Julia programming language, in order to understand the response of the detector, the function of the electronics and the physical events. In this thesis two types of analysis methods have been used, namely the DAQ Energy method and the more rigorous DSP (digital signal processing) method. While energy values are extracted in DAQ, the DSP analysis has more steps, because it needs to process events more carefully, by looking at individual waveforms and their properties.

First of all, using the DSP method raw waveforms were analysed. They represent the physical events detected. A waveform consists of three parts:

- Baseline (The baseline contains no detector signal, but non zero values are information about the leakage current. Also the higher frequency variation from the mean baseline value can be used as a measure of the noise.)
- Rising edge (The rising edge the exact shape of this edge displays the way how the charges moved through the detector before reaching higher field areas [38].)
- Falling edge (The falling edge is caused by the reaction time of the electronics and usually has the shape of an exponential decay curve.)

These parts are shown in figure 21 with an example of a waveform from the polished lithium contact for a better understanding:

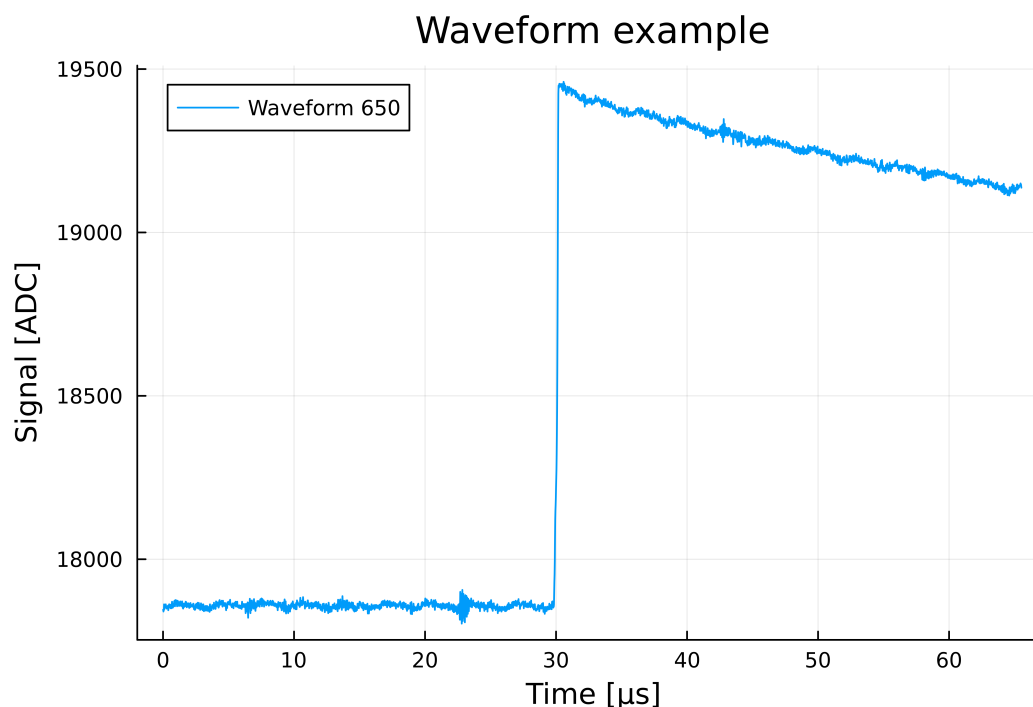


Figure 21: Example of a waveform with baseline (region ranging from the origin of the plot to short before $t=30 \mu\text{s}$), rising edge (steep rise around $t=30 \mu\text{s}$) and falling edge. Here only moderate amounts of noise can be seen

There are several steps of DSP (digital signal processing) analysis that have to be performed on waveforms, in order to correctly extract the energy from them. Firstly, one would arrange the baselines by performing a subtraction. Furthermore, a linear model is used to fit the falling edge part of the function. Then, the part of the waveform that is not in the region of interest is eliminated by applying a selection filter on the respective values.

The most important analysis steps are summarized:

- **Baseline subtraction:** The baseline of the waveform is corrected for the ADC offset in order to look at physical events and extract the decay time of the electronics. The baseline subtraction is effectuated by subtracting the average value in order to evaluate the amplitude of the baseline independent of the ADC offset. In addition, with data of the baseline, one can investigate properties for more parameters, such as the baseline mean value, the slope of the baseline and its standard deviation. These parameters are useful for quality cuts of the spectrum [22]
- **Decay time computation:** this step aims to calculate the decay time constant. To deconvolute the waveform from its exponentially decaying tail induced by resistive-feedback readout electronics, a precise value of the decay time (τ) needs to be determined. In a first step, the decay time is computed individually for every event. Assuming that the decaying tail can be described by an exponential of the form $x(t) = A \cdot e^{-\frac{t}{\tau}}$, where A stands for the amplitude and τ the time, the decay time is obtained by fitting a linear function of form $C \cdot x + f$ to the logarithm of $x(t)$. The decay time (τ) is an important pulse shape parameter since it provides information on the stability of the readout electronics. τ is approximately the product of the feedback resistance R_f and the feedback capacitance C_f , ($\tau \approx R_f C_f$ [22]). Next, one can deconvolute the waveform to remove the electronic response of the RC-feedback loop in the Charge Sensitive Amplifier (CSA). If one has extracted the decay time constant, the deconvolution can be performed with the inverse CR filter and the decay time constant as argument.
- **Energy filter:** the energy can be extracted from the signal shaped by a trapezoidal filter. This filter uses more parameters, such as the trapezoid rise time or the trapezoid flat top. One needs to choose a sufficiently long flat top time to accomplish complete charge integration and enough long rise time to blend high-frequency noise away [17]. By using a fixed-time-pickoff (ftp), the rise time is extracted at a fixed time point relative to the onset of the charge collection t_0 , e.g. at the center or maximum of the flat top region. The use of the trapezoidal filter is shown in figure 22.

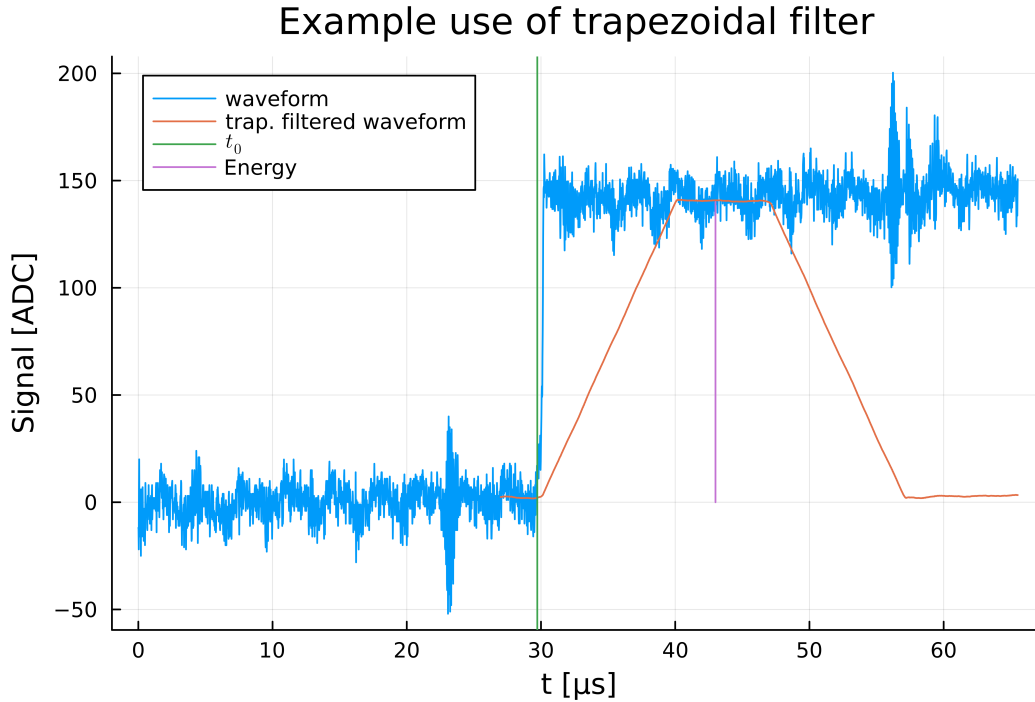


Figure 22: Applying a trapezoidal charge filter to a noisy waveform, where the energy is read out as the height of the filtered trapezoid and the calculated time of charge collection is also displayed

After obtaining all the energy data extracted from the waveforms, one only needs to plot a histogram (usually using a logarithmic scale) to obtain the sought after spectrum. In figure 23 one will remark a difference between two spectra, namely the raw one which is displayed in blue (containing no quality cuts) and the one after quality cuts (displayed in orange).

The quality cut is performed in order to further filter and select relevant data. This is realised by filtering the energy values after some parameters, such as the mean value of the baseline, the slope and its standard deviation. The first two parameters are estimators for the stability of the detector leakage current and the electronic noise, and the baseline slope is a proxy for pre-trace pile-up. This type of pile-up is a superposition of the exponentially decaying tail of the previous event and the baseline of the actual waveform [22]. These parameters are plotted and then only the values that are in the peak of the normal distribution are being kept, while the events corresponding to the other values are rejected. This procedure enables a more rigorous analysis and yields a cleaner spectrum.

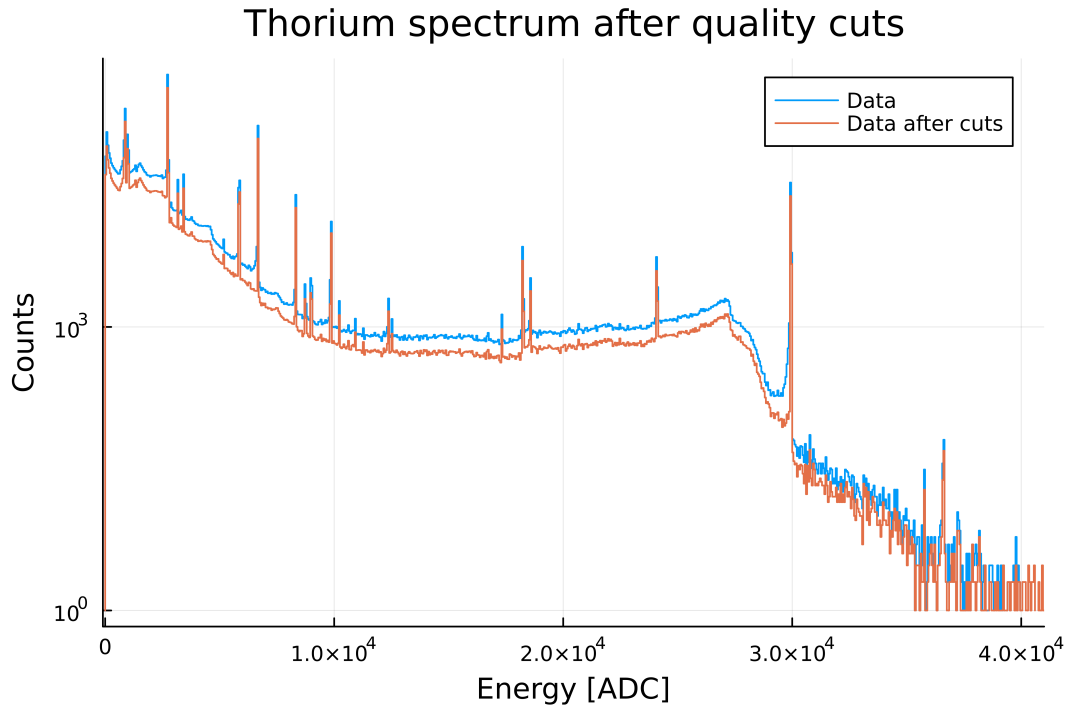


Figure 23: ^{228}Th spectra: comparison of the spectrum formed with raw data (plot in blue) and the one after quality cuts imposed on baseline parameters (in orange). One will notice a cleaner form after quality cuts, but also a reduce in the number of counts, due to less amount of data.

In order to start the steps of the DSP analysis, one needs to look at the individual waveforms from the datafiles. In general, one datafile contains hundreds of thousands of waveforms. Therefore, series of individual raw waveforms from all measurement campaigns with the contacts were plotted and their form was analysed. This gives one an insight, about how the detector and its electronic components are responding to the physical events. The most interesting waveforms will be displayed from figure 24 to 29, i.e. waveforms that exhibited some particular behaviour or reflected the general behaviour of the detector in the measurement on that contact.

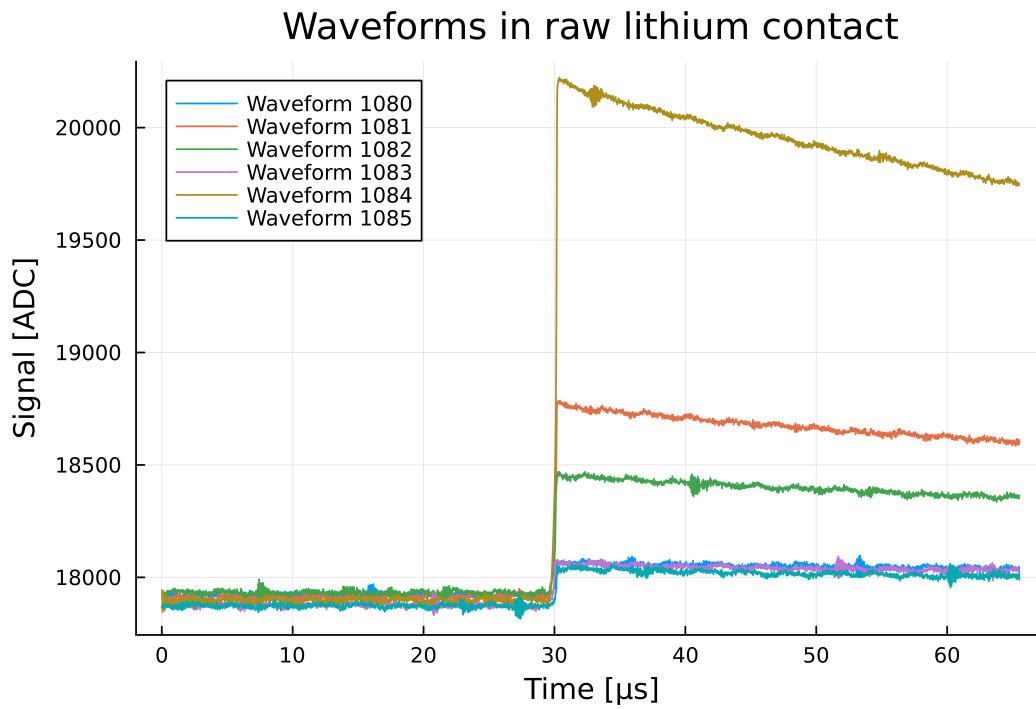


Figure 24: Example of waveforms in raw lithium contact during the calibration procedure with ^{228}Th

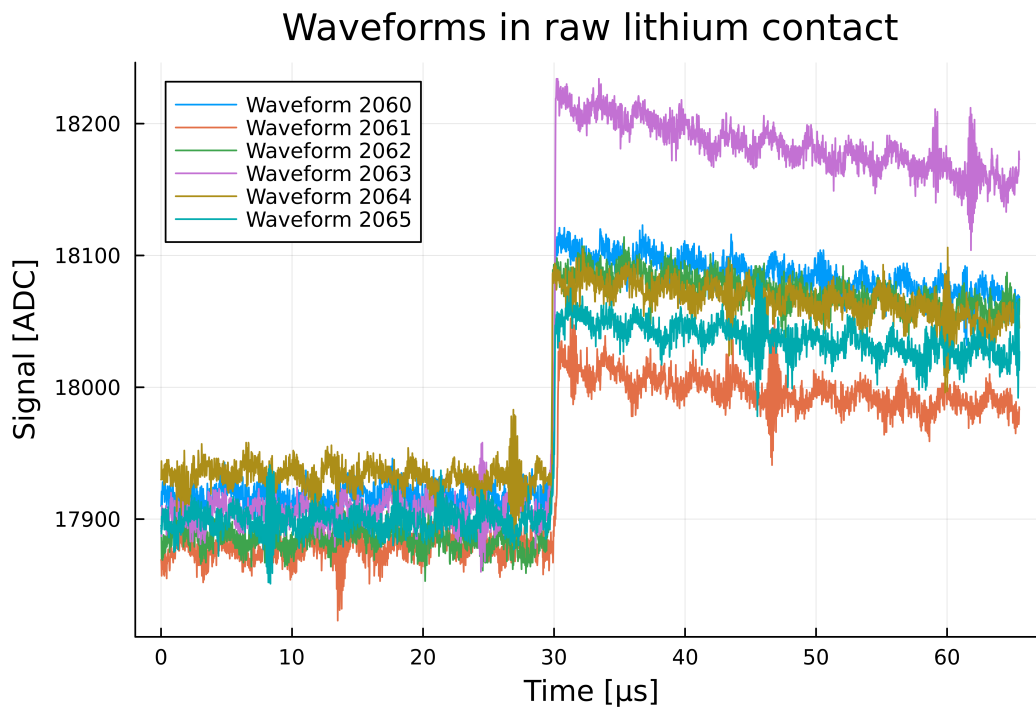


Figure 25: Example of waveforms in raw lithium contact during the calibration procedure with ^{228}Th

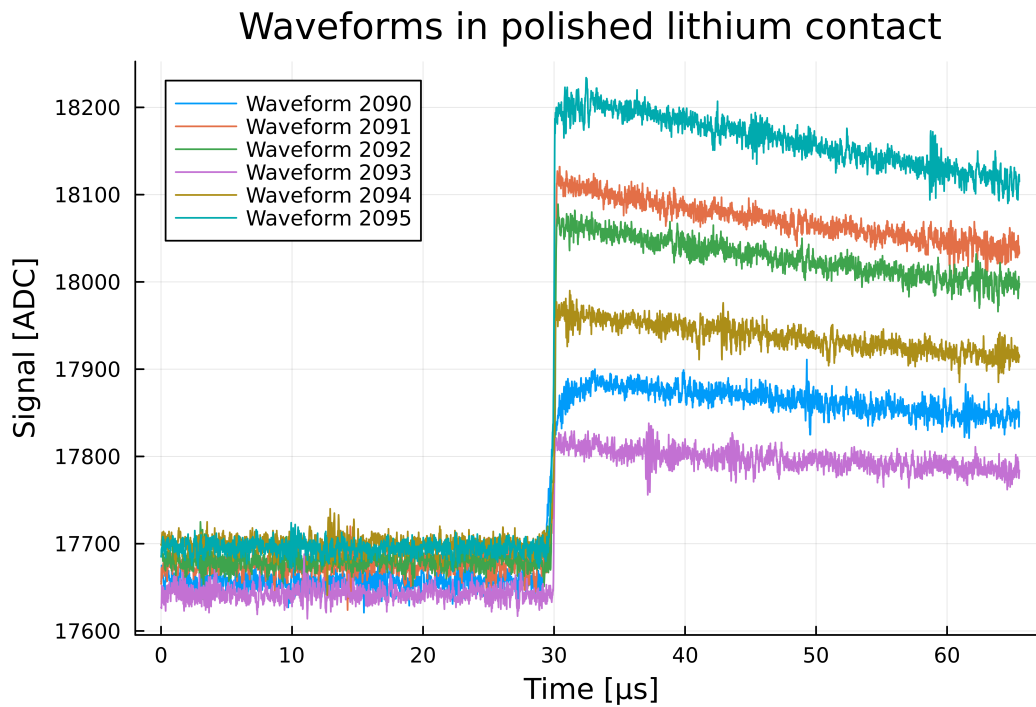


Figure 26: Example of waveforms in polished lithium contact during the calibration procedure with ^{228}Th

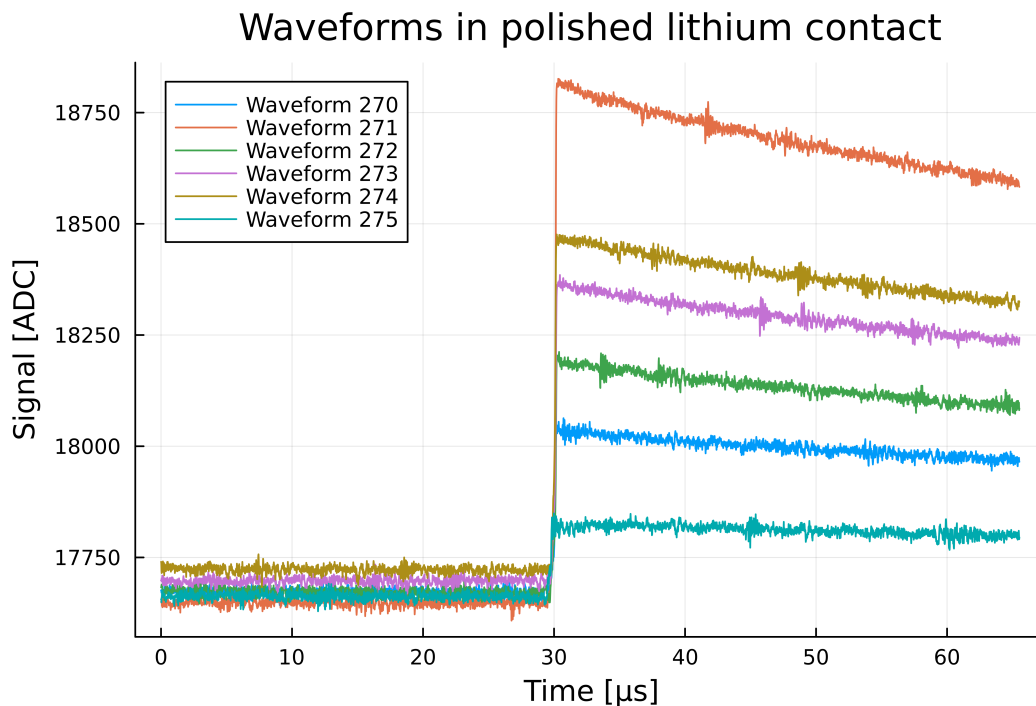


Figure 27: Example of waveforms in polished lithium contact during the calibration procedure with ^{228}Th

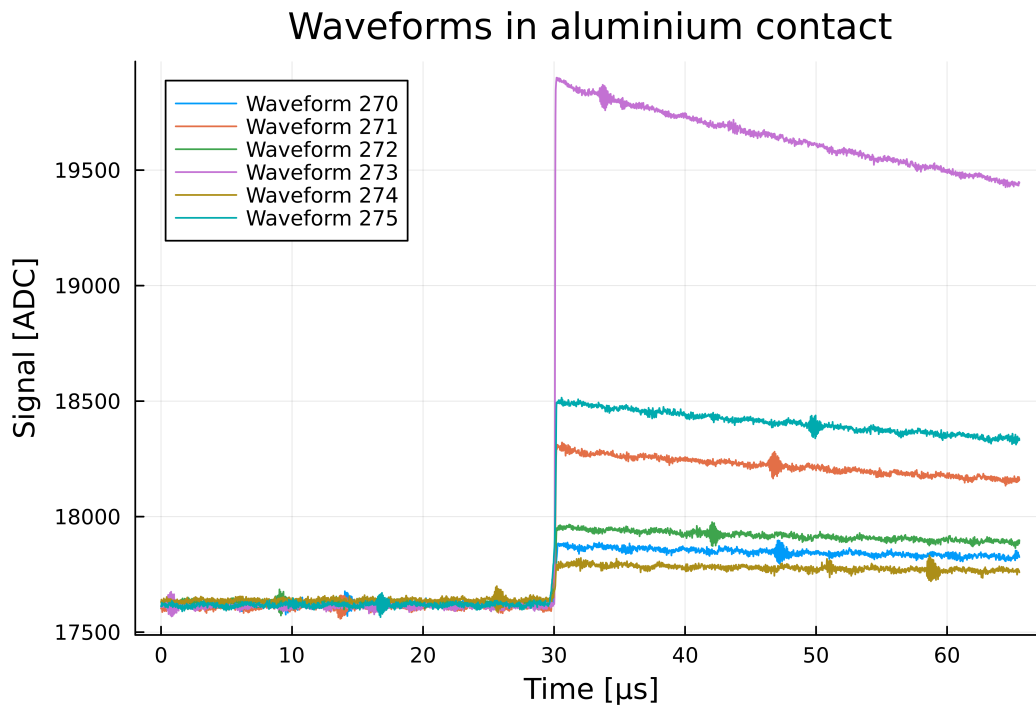


Figure 28: Example of waveforms in aluminium contact during the calibration procedure with ^{228}Th

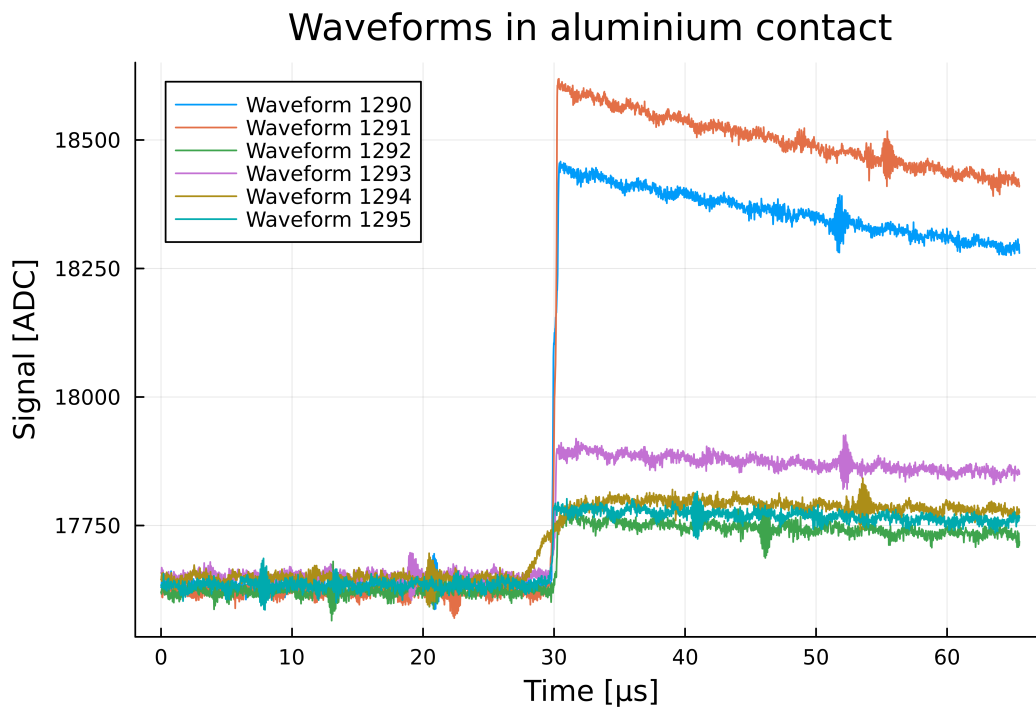


Figure 29: Example of waveforms in aluminium contact during the calibration procedure with ^{228}Th

In figures 24 to 29 individual raw waveforms have been selected, two set of five waveforms for each contact. Regarding the form of the waveforms, all of them have the expected shape with baseline, rising edge and falling edge, representing physical events registered by the detector. Waveforms which did not have this shape were eliminated in the analysis procedure, since they did not represent physical events, but background interactions such as responses of the electronic system or surface events in the detector.

At a closer look, one will notice that most waveforms exhibit higher fluctuations in the baseline and falling edge, suggesting that the detector was operated in the laboratory under noisy conditions. This electrical noise might have been caused by the light system, other electronics used or experiments running nearby in the same room.

In the raw lithium contact, the waveforms 1080 to 1085 from figure 24 are of an adequate quality, with a modicum of noise, see the spikes at waveform 1084 and 1082 in the falling edge. Figure 25 represents the case with more noise and lower amplitudes, where higher noise levels can be observed. Both the baseline and falling edge of the waveforms in fig. 25 present an alternating behaviour, resembling a sine curve.

Generally, the waveforms in the polished lithium contact had smaller signal amplitudes, suggesting a weaker performance of the detector on that particular contact. This observation will be addressed in the spectroscopy analysis chapter. In figure 26 one can see a sample of waveforms dominated by noise, in contrast to the samples in figure 27. Particularly, the convexity at the beginning of the falling edge is altered for waveform 2090 and waveform 2095.

For aluminium, the waveforms in figure 28 and 29 present moderate levels of noise, with local spikes. The waveform 1294 in figure 29 is of particular interest, since it has a different shape of the rising edge and a slower rise time. Such a waveform represents an alpha surface event, where the phenomenon of delayed charge recovery happens. In this case, charges are collected on the passivated surface of the detector and re-released after a certain time in the bulk region of the detector again [22].

As comparison, one can already visually remark that the selected waveforms possess distinct features and differ from one contact to the other. This fact will lead to different results in the spectroscopy analysis of chapter 8. As a common feature, all waveforms have a significant amount of electronic noise in their baseline and decay curve.

8.2 Analysis on contacts

A fundamental detail of the analysis with the spectrum is the energy conversion, where one goes from the ADC units to the physical units. This is done by using a linear conversion relationship, normally starting with the full energy peak. One extracts the ADC value x_{peak} from the spectrum and uses the following equation when performing a simple calibration on the full energy peak:

$$E[keV] = E[ADC] \cdot \frac{2614.511keV}{x_{peak}} \quad (17)$$

However, for a real and accurate calibration a linear function is used to convert ADC

units to keV:

$$E[\text{keV}] = a \cdot E[\text{ADC}] + b \quad (18)$$

After calibrating the energy by making use of the most prominent peaks with the linear conversion formula for each of them, the following thorium spectrum was obtained in figure 30:

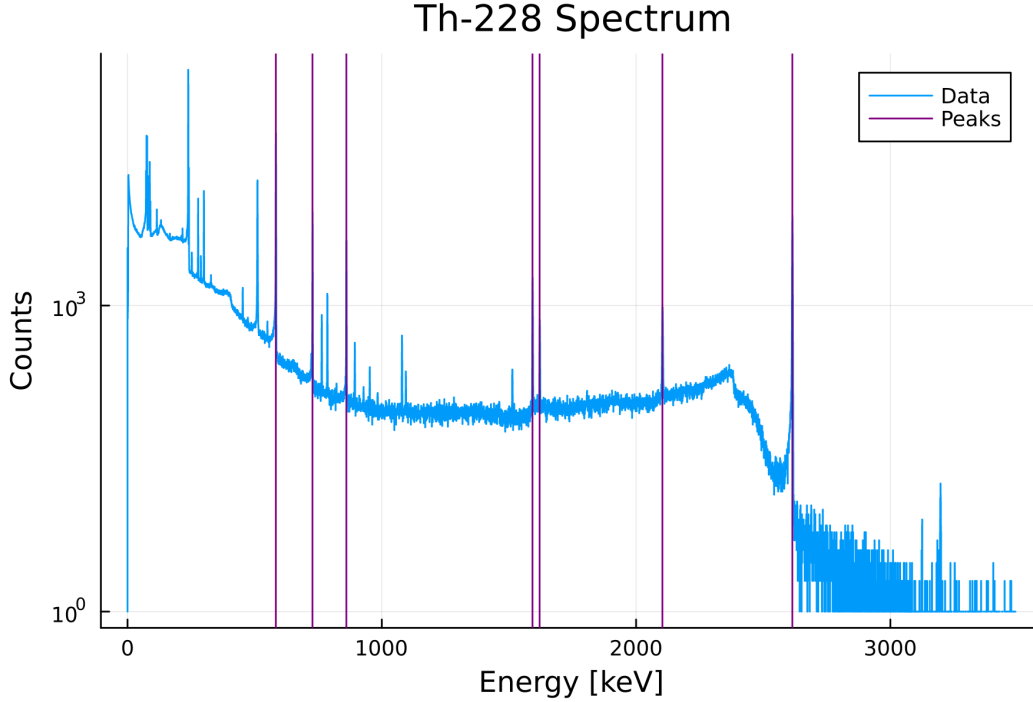


Figure 30: ^{228}Th spectrum with vertical lines at specific peaks listed in table 5 and all specific features, including the Compton edge

with significant peaks [17]:

Table 5: Energy, Element, and Name Data

Energy	Element	Name
583.191 keV	^{208}Tl	-
727.330 keV	^{212}Bi	-
860.564 keV	^{208}Tl	-
1592.53 keV	^{208}Tl	double escape peak (DEP)
1620.50 keV	^{212}Bi	full energy peak (FEP)
2103.53 keV	^{208}Tl	single escape peak (SEP)
2614.50 keV	^{208}Tl	full energy peak (FEP)

Some of these peaks have interesting properties, regarding the behaviour of the photons. Namely the so called full energy peak (FEP) is a signature for events where the whole energy of the incident photon is absorbed in the active volume. Then, the single escape peak (SEP) is the signature of events, where only one of the photons produced during annihilation of electrons with positrons escapes the active volume, while the double escape peak (DEP) is the one where both annihilation photons escape the active volume.

The Compton edge is the steep line before the last peak, characterized by the the maximum deflection angle of the incident photon under Compton scattering. Events in the spectrum after this edge are caused by multiple Compton scattering. [17]

Furthermore, a zoom was performed on the significant peaks, in order to see their shape and verify the quality of the spectrum in the region of interest. The ideal case would be a perfect Gaussian peak, however real data contains noise and needs further processing. The next step was performing a Gaussian fit in Julia on the peaks, in order to extract the standard deviation and mean value. In the next figure, one can see the Gaussian fit function performed only on the data from the full energy peak.

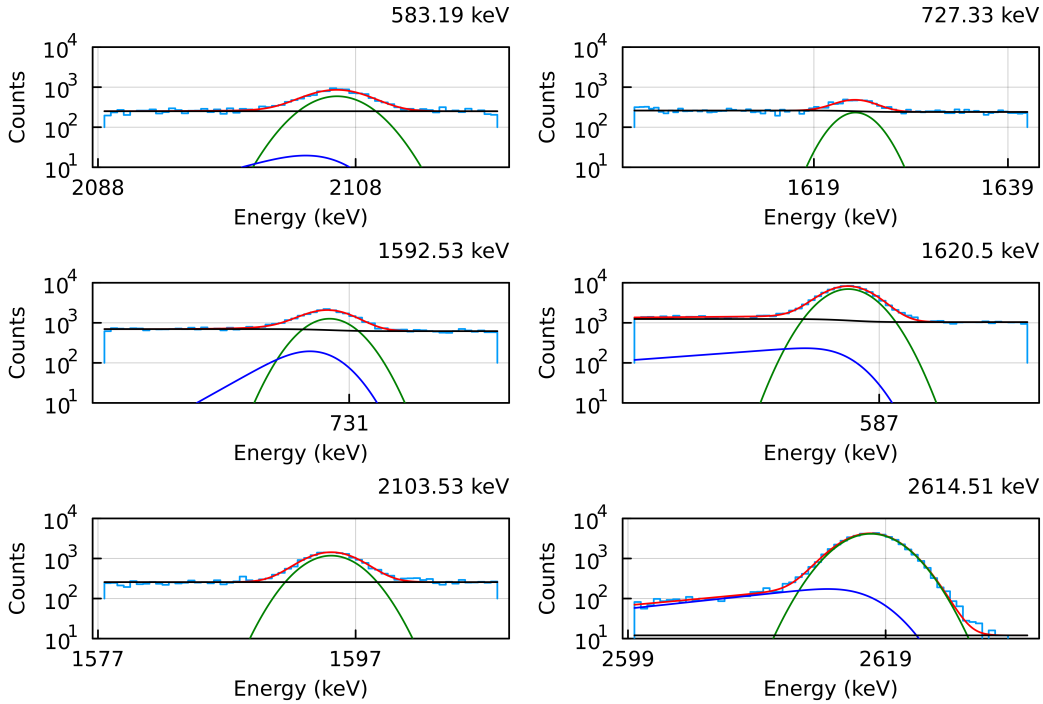


Figure 31: Elaborated fit on the region of the significant peaks using a gaussian (green curve) , a low-energy step (dark blue curve), a constant background (black curve) and an low energy tail (orange curve)

For a more detailed analysis of the peaks, one needs to take into account a more realistic model, than the often idealized gaussian. In the result section, the fits on the peaks will be done through an algorithm that uses a function composed of more parts: a gaussian, a low-energy step, a constant background and an low energy tail, exactly as in figure 32. Such a function can be parameterized the following way [17]:

$$f(E) = A \cdot \exp\left(-\frac{(E-\mu)^2}{2\sigma^2}\right) + \frac{B}{2} \cdot \operatorname{erfc}\left(\frac{E-\mu}{\sqrt{2}\sigma}\right) + C + \frac{F}{2} \cdot \exp\left(-\frac{E-\mu}{\delta}\right) \cdot \operatorname{erfc}\left(\frac{E-\mu}{2\sqrt{\sigma}} + \frac{\sigma}{\sqrt{\delta}}\right) \quad (19)$$

where μ represent the value of the peak position, σ the standard deviation of the normal distribution and δ the decay time constant of an exponential, while the parameters A, B, C, and F are normalization factors. Then, the maximum from every centered peak (in ADC units) is taken and calibrated on energy with a linear fit function displayed in the next formula:

$$E[keV] = a \cdot E[ADC] + b \quad (20)$$

As a next step, one is seeking to determine the performance of the detector with respect to the energy resolution. This is usually defined as the energy resolution at the full width at half maximum of each peak (FWHM). Usually the FWHM for a gaussian distribution is approximated with the following formula:

$$FWHM = 2\sqrt{\ln 2} \cdot \sigma \approx 2.355 \cdot \sigma \quad (21)$$

Because of the high statistics and noise considerations, the function chosen for the fit of the FWHM as a function of energy was the square root from a linear function:

$$f(E) = \sqrt{a \cdot E + b} \quad (22)$$

This function builds a satisfying description of the fit, since the noise uncertainties are computed over their components. The energy resolution of a high purity germanium detector is composed of three statistically uncorrelated terms: the ENC noise (equivalent noise charge), the statistical fluctuations in the charge production process (Fano limit) and the efficiency of the charge collection process in the crystal and the electronic system [33]. The Fano factor is a correction parameter to account for typically higher-energy resolution than predicted from pure Gaussian statistics [33]. The formula used for the energy resolution can be written as [29]:

$$FWHM(E) = 2\sqrt{2} \cdot \log 2 \cdot \sqrt{\frac{\eta^2}{e^2} ENC^2 + \eta F \cdot E + c^2 \cdot E^2} \quad (23)$$

where η represents the average energy to create an electron-hole pair in germanium-76, while the fraction $\frac{\eta}{e}$ refers to the voltage produced at the readout of the detector per elementary charge e which was measured inside the bulk. Further ENC represents the ENC noise, F the Fano factor, E the energy and c is a constant.

In the Figure 32, one can see the conversion linear fit from the digital ADC units to the physical keV units, used to calibrate the spectrum. The data points correspond to the significant peaks of the spectrum. In this plot, one can see that the formula works for the calibration, since it is a good fit for the curve. In the next figure, Fig. 33, a square root function was fitted on data points, consisting of the peak values and their full width half max, in order to obtain the energy resolution of the detector and compare it to LEGEND values. This plot takes into account the energy of the peaks at FWHM and also their energy resolution. In figure 33, one can observe that the energy resolution of the peaks was parameterised with a square root function like the one mentioned in equation 22. This serves as a general example of fit for the energy resolution of the peaks against their original energy. This measurement and analysis was performed during a standard ^{228}Th calibration of the BEGe detector in the same conditions as the measurements described in section 6.3, but this time with a well functioning electrical contact. Therefore, the energy resolution is having a good value, namely 2.11 keV. Here, only the SEP peak was excluded from the analysis, because of its Doppler broadening.

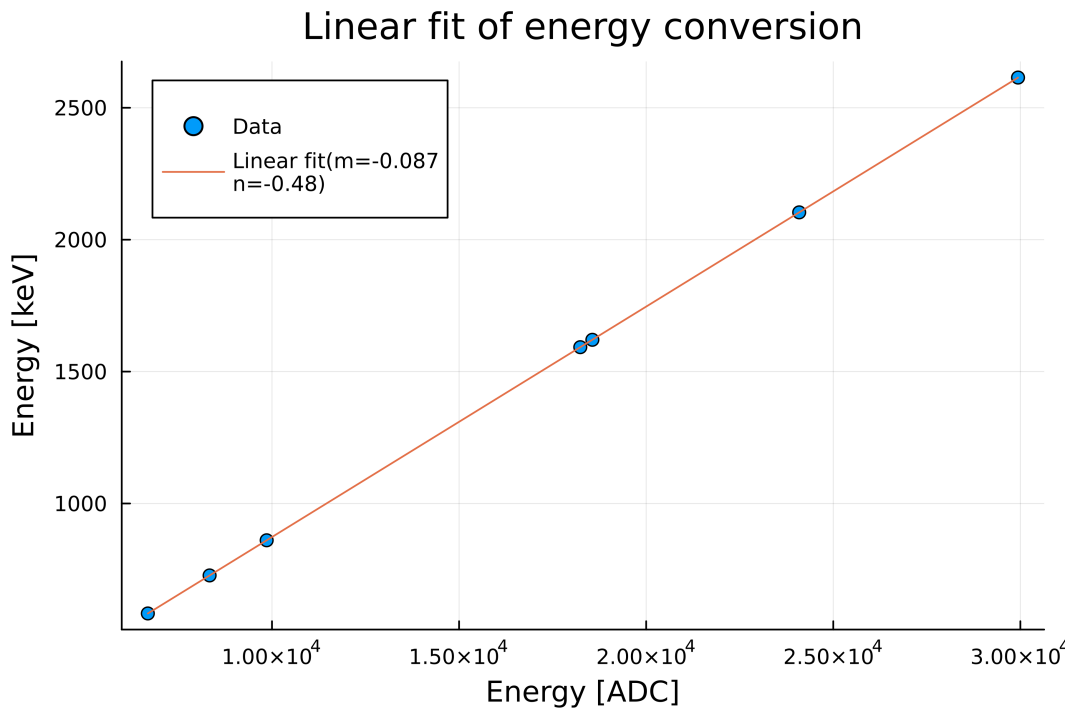


Figure 32: Energy calibration fit function for unit conversion from ADC to keV

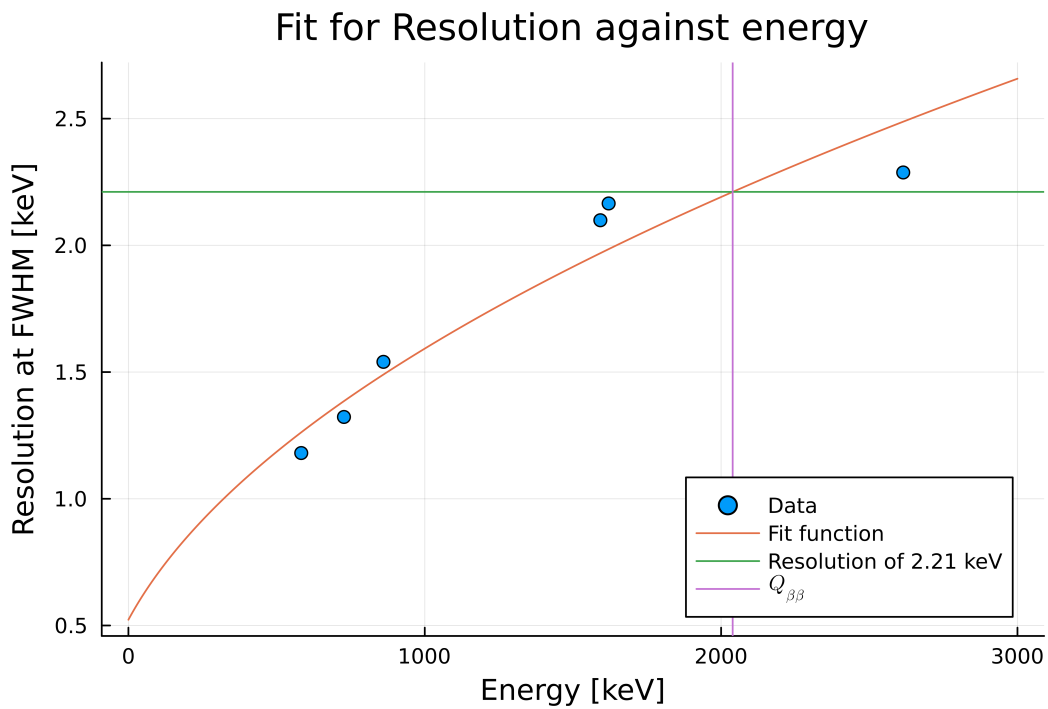


Figure 33: Energy resolution of the peaks at FWHM and the resulting fit function. For comparison with legend, a vertical line was drawn at the value of interest.

8.2.1 Aluminium contact

After measuring with the germanium detector fully depleted and cooled in a can with liquid nitrogen ($V = 68.8L$) at $T = 77K$ via the aluminium contact for approximately twenty six hours with the bias voltage of $V_B = 2500V$, the following spectrum was obtained:

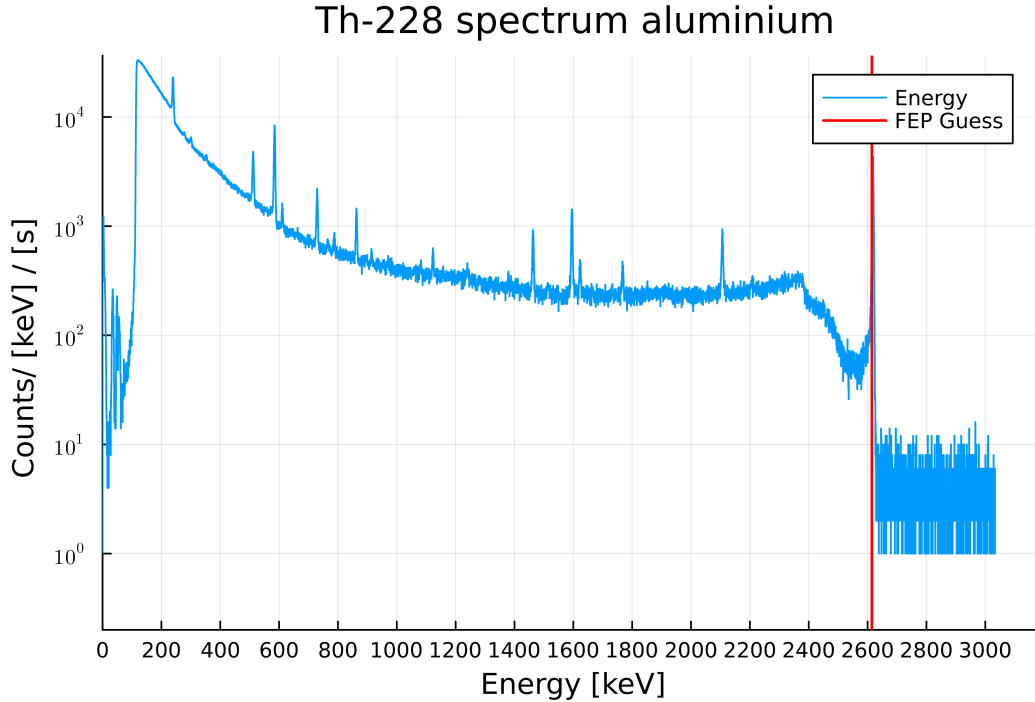


Figure 34: Calibrated ^{228}Th spectrum for the measurement at the aluminium contact

The spectrum in figure 34 shows, that the detector was functioning well, being able to identify all significant peaks for the element, regardless of the high lithium contact resistance. Furthermore, the linear calibration algorithm has correctly done the calibration after looking at the FEP peak in the spectrum, at 2614.5 keV. This proves that the energies in the spectrum lie in the correct range. The quality of the spectrum can be also viewed in the next plot, Fig. 35, where the six significant peaks are analysed in detail and fitted with the function described in section 5. When zooming on the peaks, one will not see a perfect gaussian curve, because the peak shape depends on the particular physical process in which the event originates.

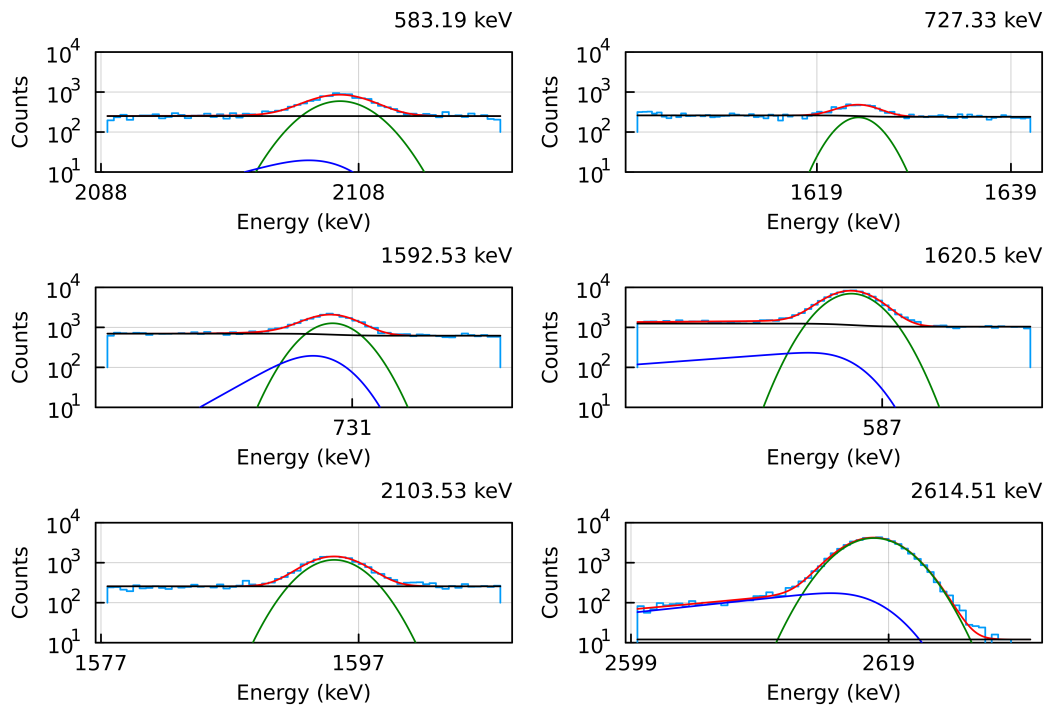


Figure 35: Fit for the peaks at the aluminium contact

So far the analysis of the aluminium contact yielded a quite good resolution of 3.74 ± 0.06 keV for full width at half max (FWHM) corresponding to the peaks.

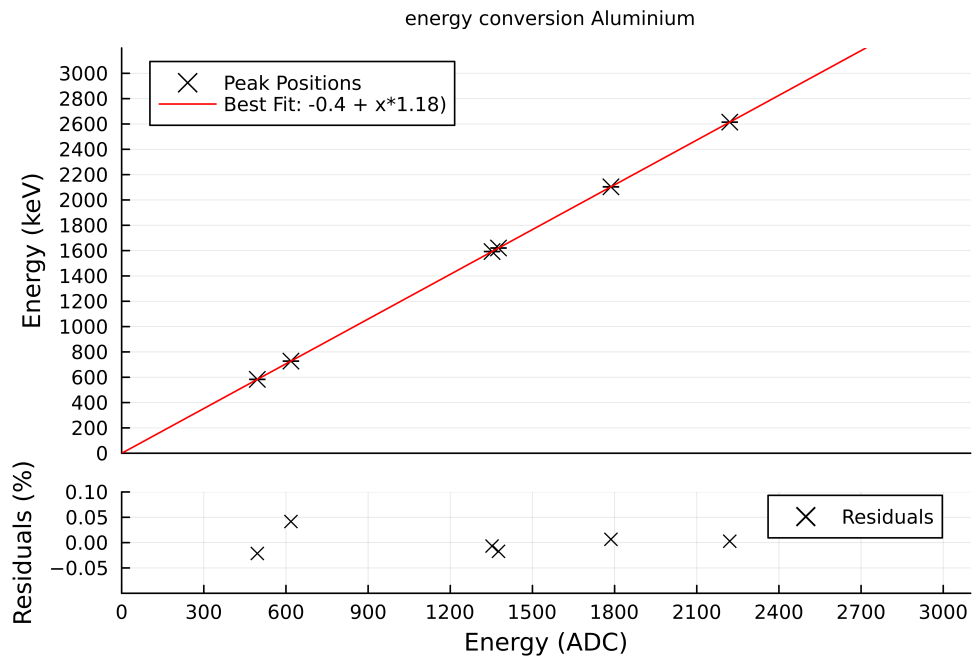


Figure 36: Energy conversion for aluminium

The linear fit in figure 36 shows how the conversion was realised between ADC units and keV units. Since the linear function fits the data points well and the residuals have small values, one can be satisfied with the calibration procedure.

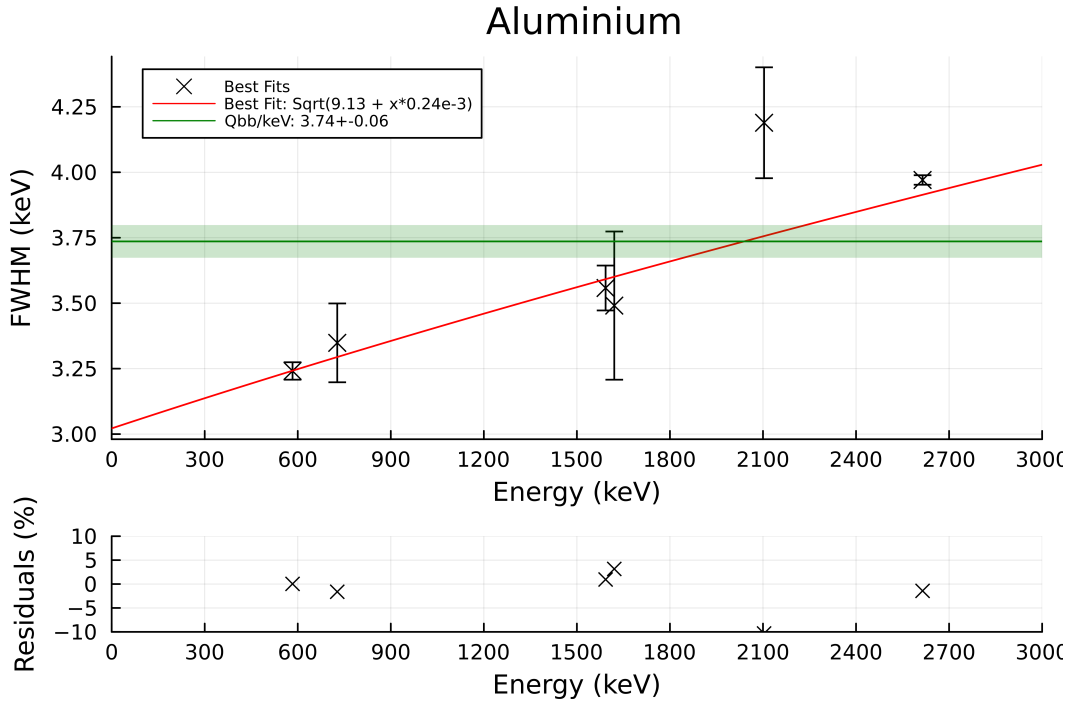


Figure 37: Energy resolution fit for the aluminium contact

This last plot in figure 37 shows a comparison between the energy of the FWHM and the energy of each peak, calculating the energy resolution of the detector. Following the standards of GERDA and LEGEND one would seek a performance of around 2-3 keV. For aluminium the results are quite acceptable, yielding a resolution of 3.74 ± 0.06 keV. One has to bear in mind, that the DEP and SEP are automatically excluded from the FWHM fit, due to their Doppler broadening effect. This effect takes place due to the Doppler shift of the gamma rays emitted.

8.2.2 Lithium contact

With the same equipment conditions and bias voltage $V_B = 2500\text{V}$, but at a different time point, the measurement via the lithium contact lasted for approximately eleven hours. As a result, the thorium spectrum looks also satisfactory, with all significant peaks being registered in figure 39. This confirms one again, that the detector and the contact were working, since the important peaks were registered. The spectrum looks very similar to the one of aluminium, yet this comparison with the spectra in the same plot will be better displayed at the end of this chapter, namely in subsection 8.2.4.

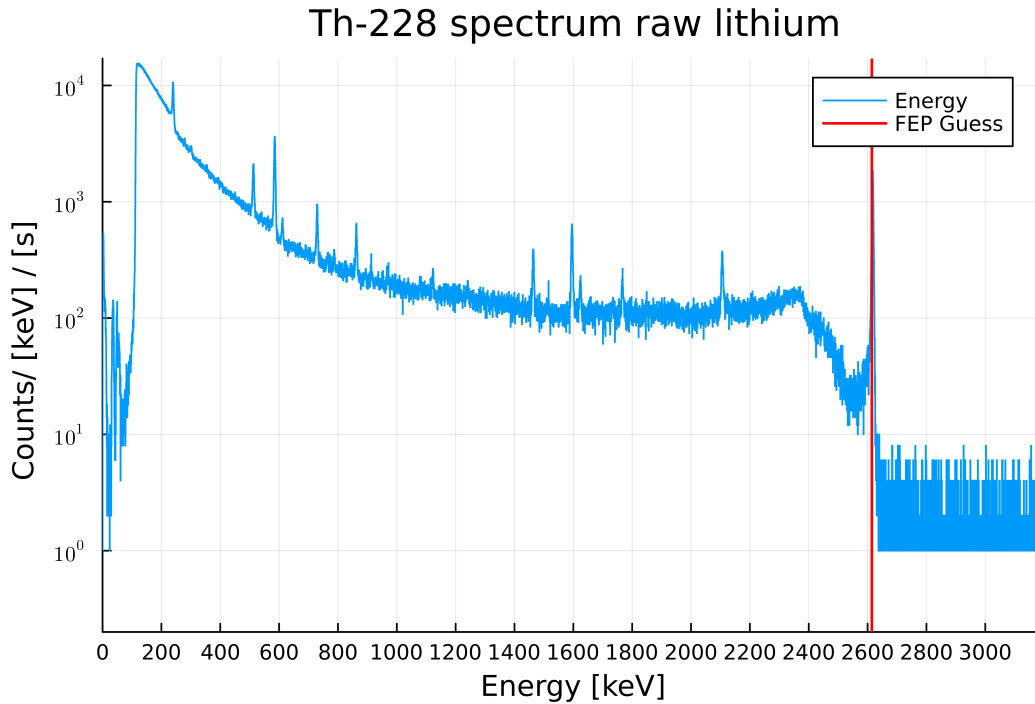


Figure 38: Calibrated ^{228}Th spectrum for the measurement at the raw lithium contact with all significant peaks and Compton edge. Furthermore, the calibration algorithm shows that it worked well, because it set the energy peaks at the right positions

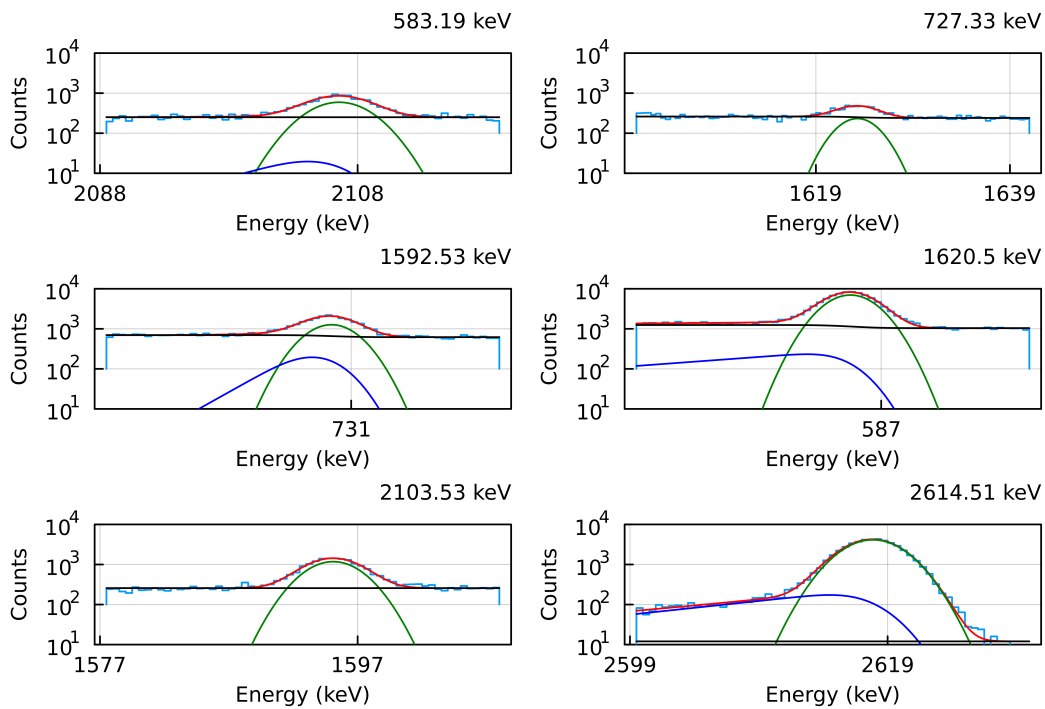


Figure 39: Peaks of raw lithium with according fit

One can observe in figure 39 that the fitting functions are working well for the peaks, with most of them having almost gaussian shapes, while the 727.33 keV and 583.19 keV peaks are also well fitted, but with a more curved baseline.

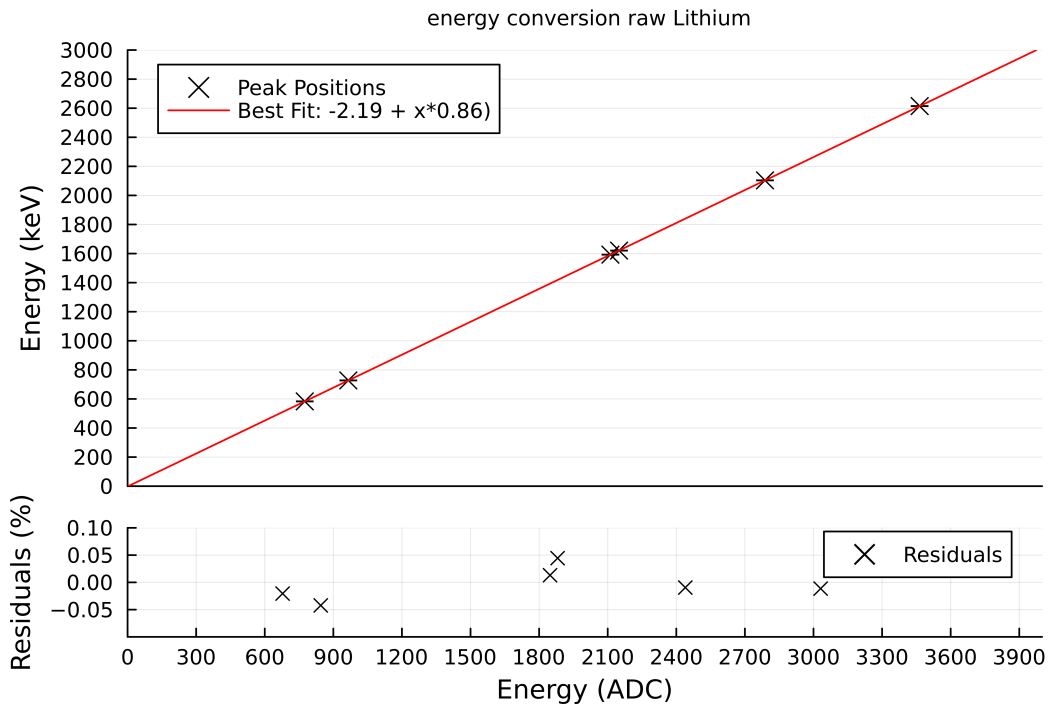


Figure 40: Energy conversion between ADC and keV on the raw lithium contact

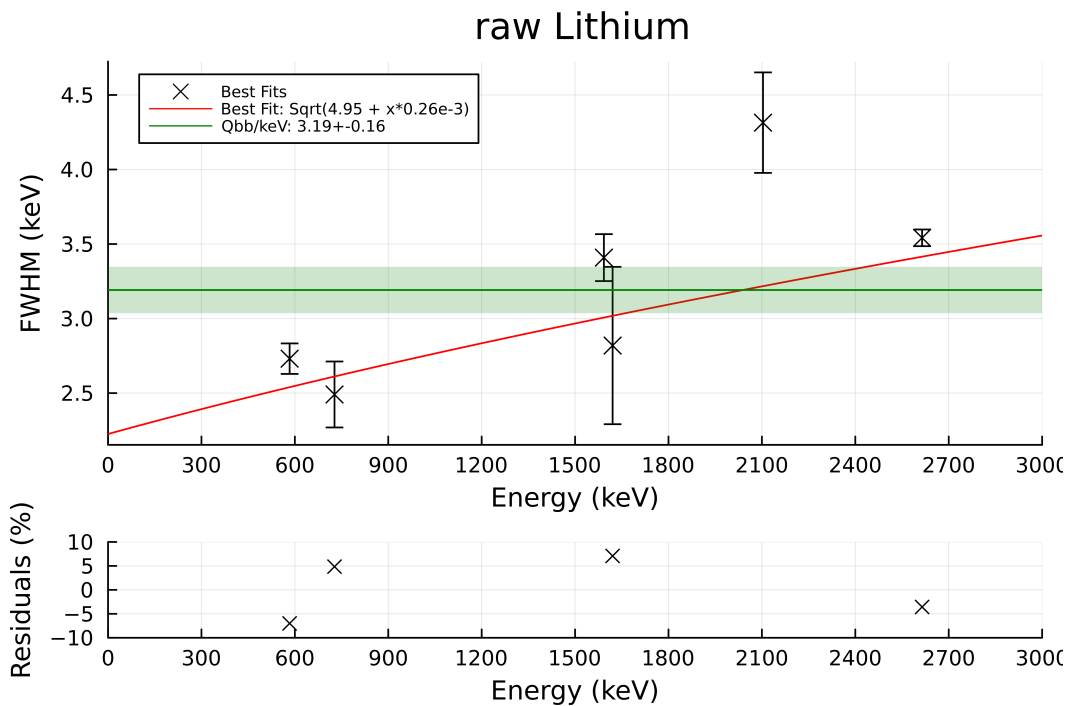


Figure 41: Fit for the lithium contact, displaying the energy resolution as a result of the resolution at FWHM extracted from every significant peak

The raw lithium contact has the best resolution from this measurement line, slightly better than aluminium and close to the LEGEND standard, namely of $3.19 \pm 0.16\text{keV}$ at FWHM stated in figure 41. Also the spectrum from figure 38 reflects a good calibration and measurement run, by identifying the fundamental peaks.

8.2.3 Polished lithium contact

Last but not least, the measurement via the polished lithium contact was done for approximately seven hours, yielding a good performance on the spectrum plotted in figure 42:

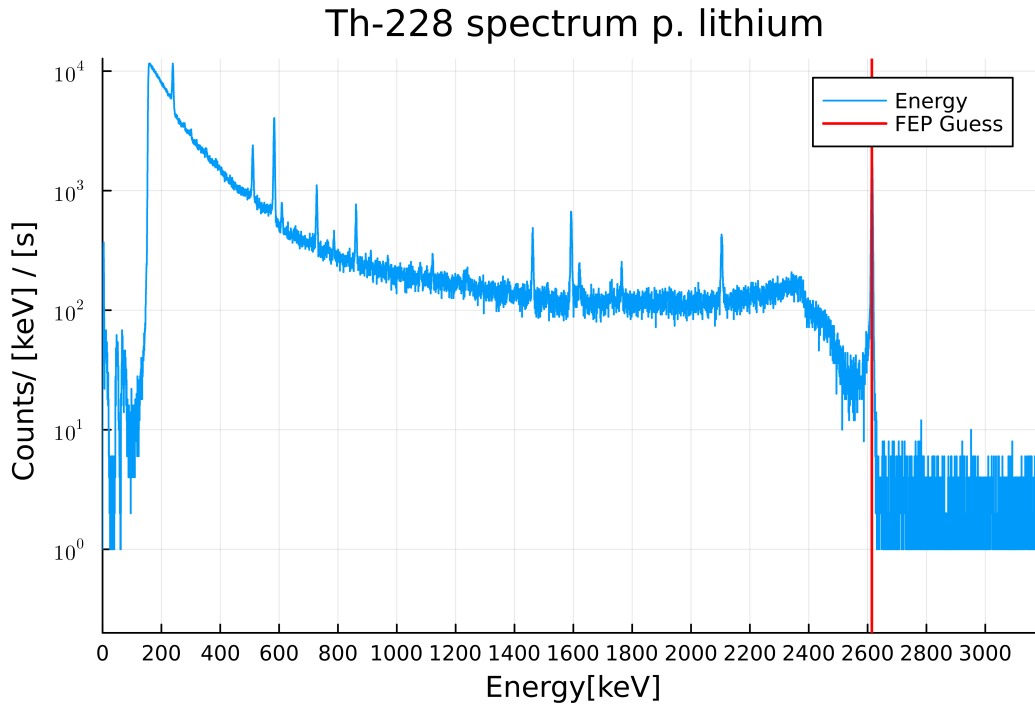


Figure 42: Calibrated ^{228}Th spectrum for the measurement at the polished lithium contact

The polished lithium spectrum in figure 42 looks also sharp, with a recognition of all important physical peaks, while correctly setting the full energy peak at its physical position after using the calibration algorithm. However, an alert reader would notice a less clean spectrum, having already from this plot more recognizable noise than the other two contacts. As a conclusion, these spectra reflect the fact that the detector was completely operational during the calibration test, presenting a shift only in the pulser, which will be shown in the next subsection.

The peaks of the spectrum measured on the polished lithium contact, in figure 43 also look satisfying, but with the exception of the 727.33 keV peak which is not so pronounced, missing the characteristic form. Generally, one could notice the tendency that the peaks form polished lithium are flatter, potentially suggesting a weaker detector energy resolution.

Further, the energy conversion data in figure 44 is also well fitted with the linear function, displaying a well scaled behaviour and small residuals.

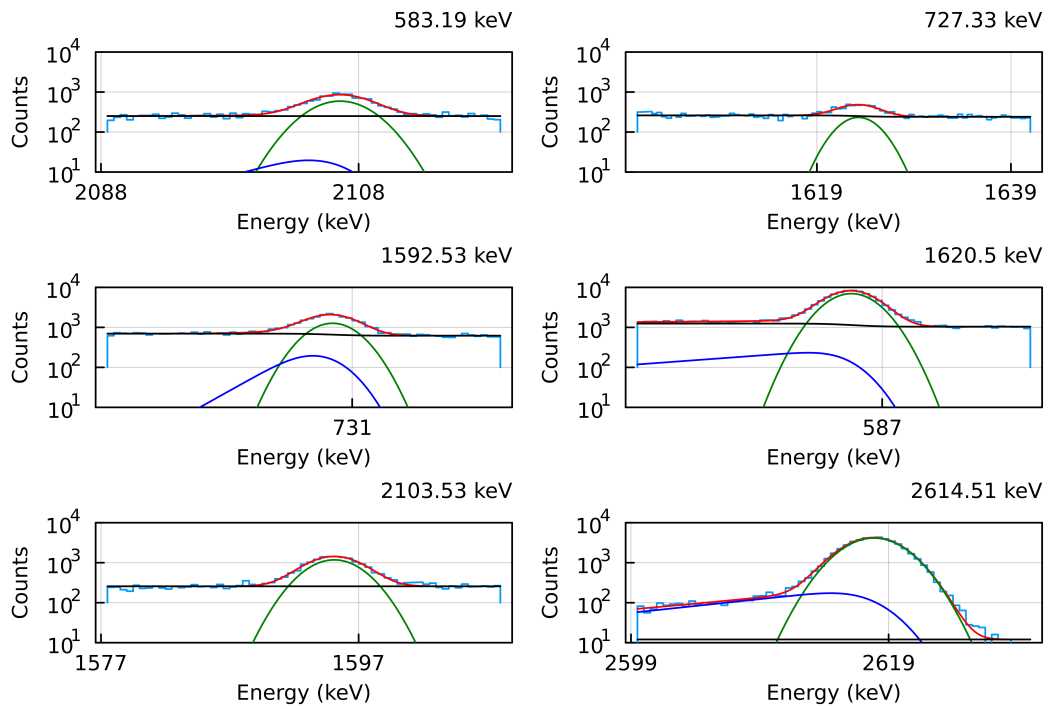


Figure 43: Fit for the peaks at the polished lithium contact

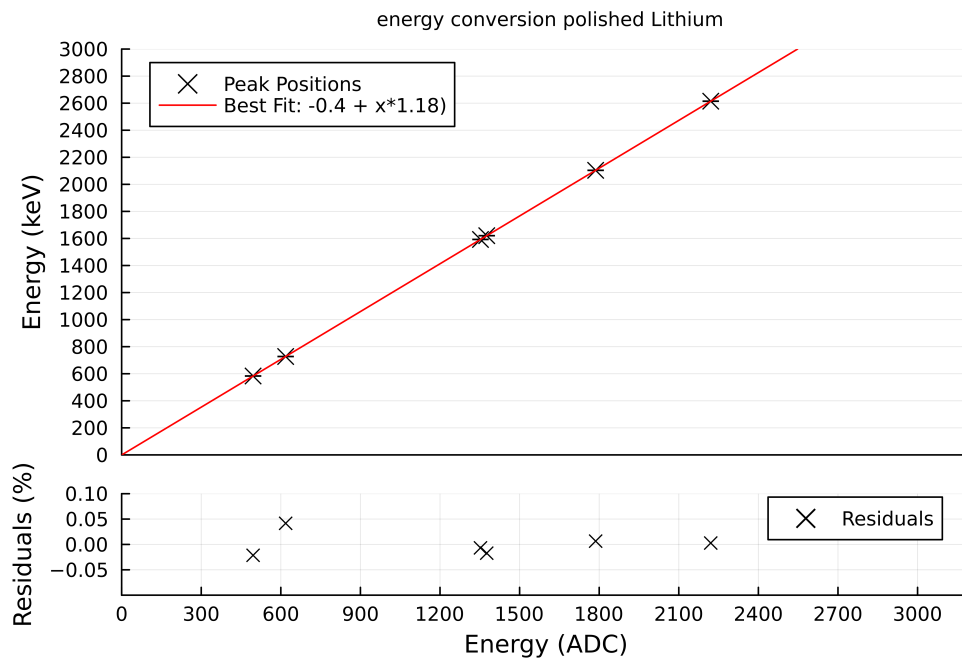


Figure 44: Energy conversion for polished lithium

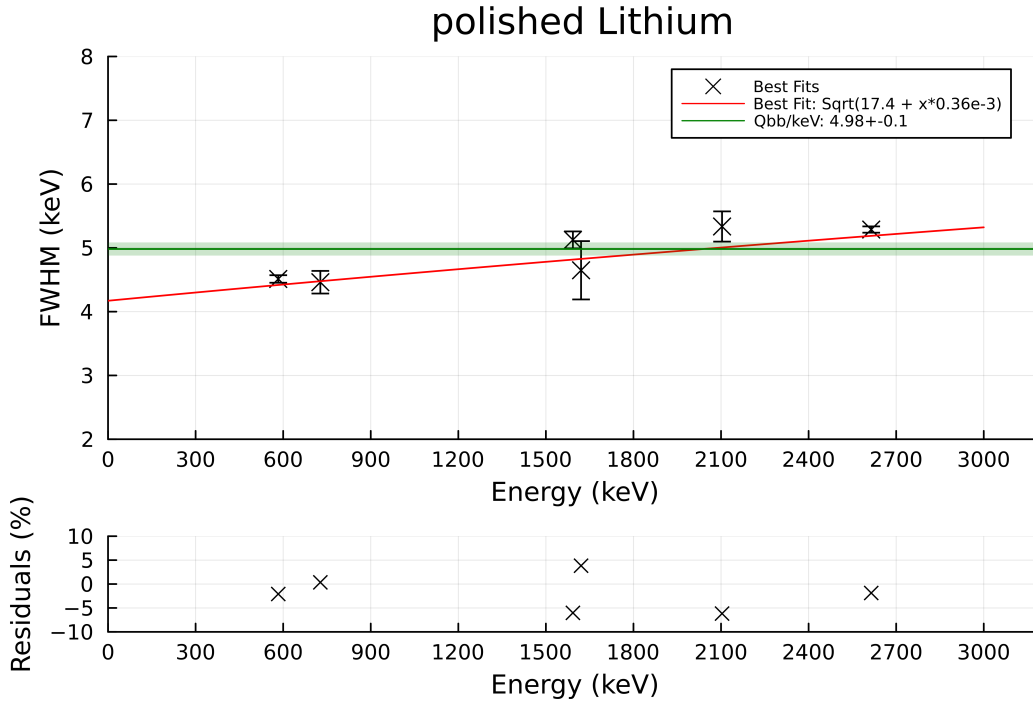


Figure 45: Energy resolution fit for the polished lithium contact

It is not surprising that the polished lithium contact performed with the poorest energy resolution, stated in figure 45 at 4.98 ± 0.10 keV at FWHM. The results of the measurement of the resistance for this contact is according to the scales of the measurements performed at LEGEND. [37]. However, the poor energy resolution can not be explained only by the higher resistance values. In the end, one has to bear in mind that the measurements have each been performed at different times. This means, that the noise levels might have been different in the laboratory for each measurement.

8.2.4 Comparison between contacts

In order to compare the performance of the detector, the thorium spectra will be plotted in one histogram in figures 46, 47 and 48. The first spectra will be presented from the data acquisition process, where no individual waveforms were processed, only the DAQ energy. In the uncalibrated spectrum from figure 47, one can see that the position of the pulsers is almost the same, while the polished lithium spectrum is shifted to the left. This shift indicated that the bad contact influences also the amplitude of the signal, since the line at 2.6 MeV has decreased in amplitude. Furthermore, some peaks originating from background events appear for all spectra around the value of 1300 ADC.

This result shown in figure 47 presents a shift of the black pulser line for polished lithium because of the performed energy calibration. The "unexpected peaks" in the thorium spectrum around the value of 1000 keV shown in picture 48 correspond to the ones mentioned and shown in figure 47. They do not represent new events or new decays. These peaks may be only caused by electronic noise or unfiltered waveforms, since they will disappear after the more rigorous DSP analysis.

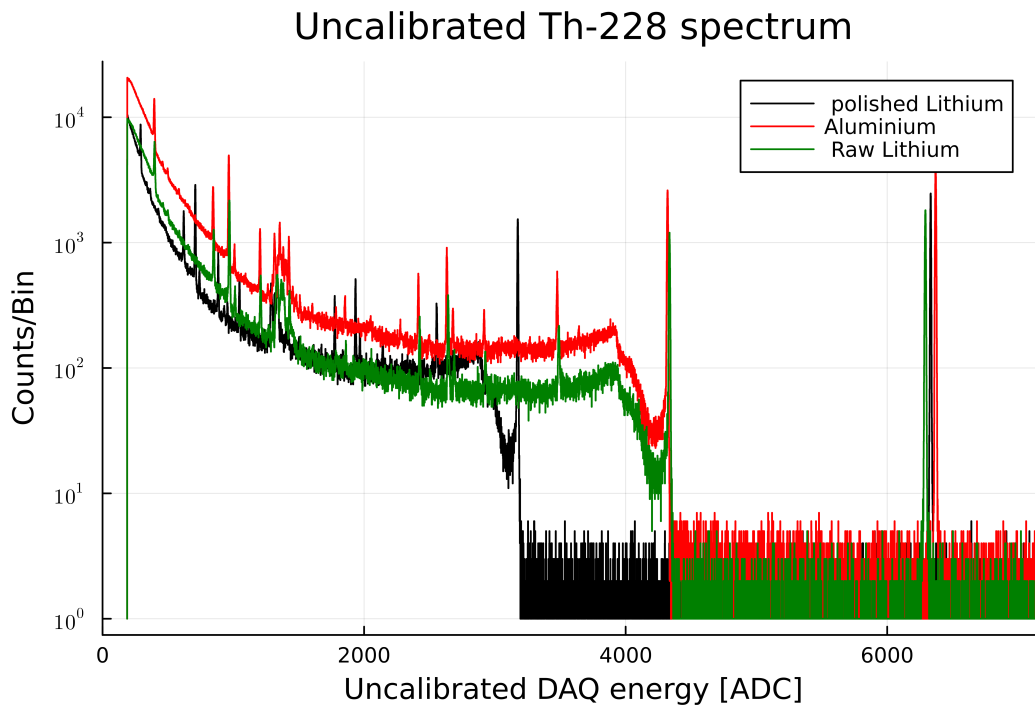


Figure 46: DAQ analysis ^{228}Th uncalibrated spectra for all contacts with the applied pulser at the end. One will remark that in the uncalibrated histogram, the pulsers are consistent to the same position, while the polished lithium spectrum has a shift to the left.

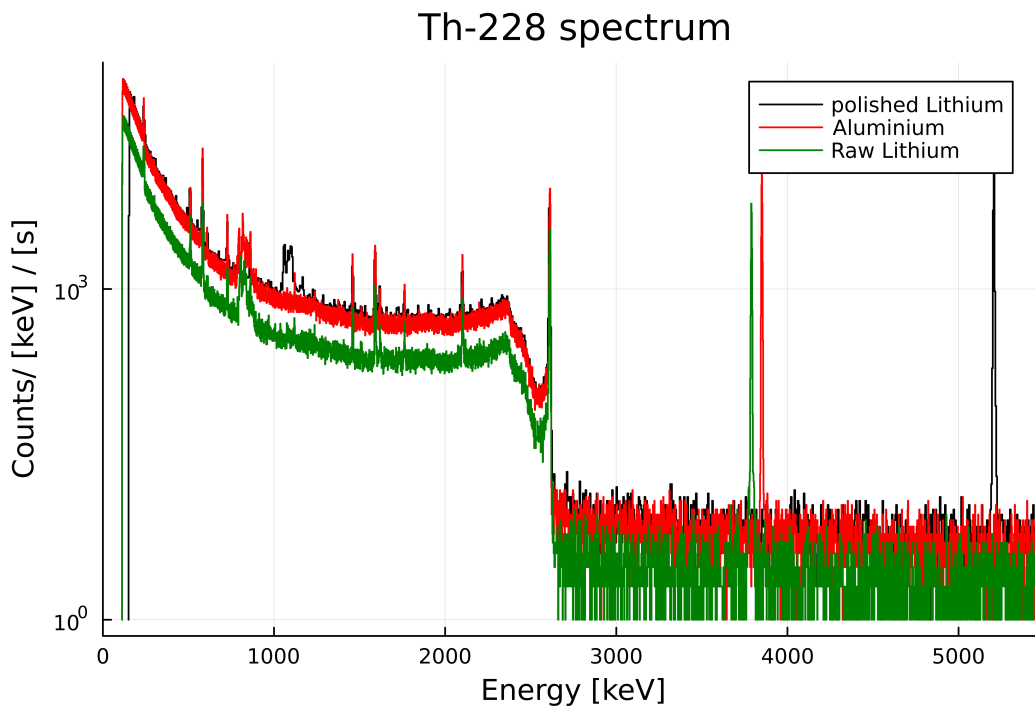


Figure 47: DAQ analysis ^{228}Th spectra for all contacts with the applied pulser at the end

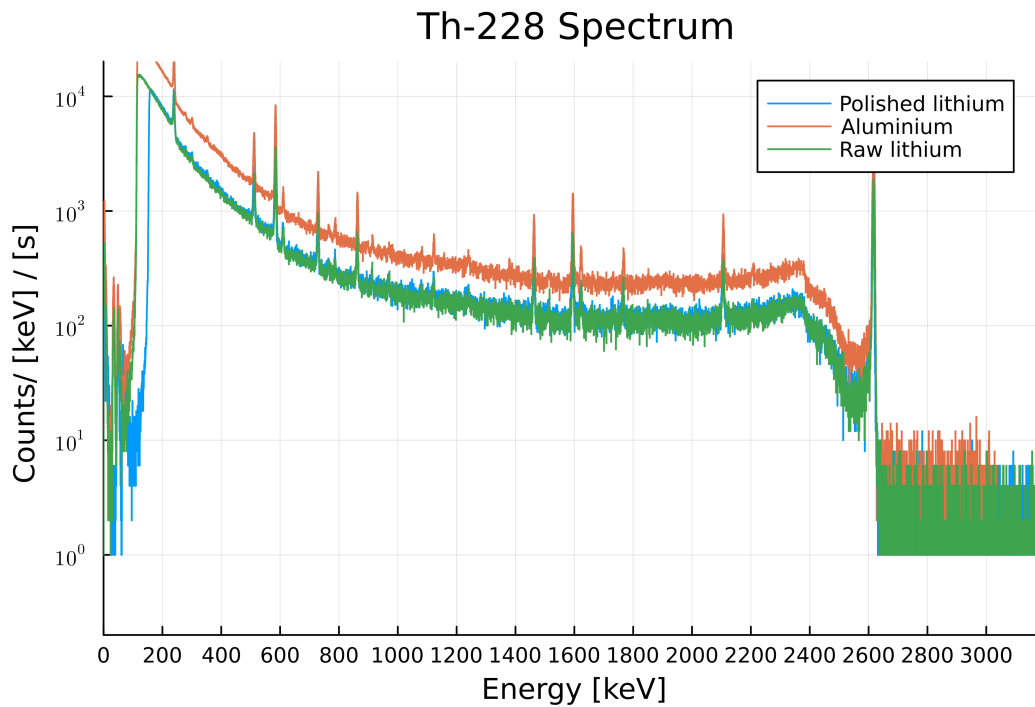


Figure 48: DSP analysis ^{228}Th spectra for all contacts in comparison of each other

In figure 48, one will observe that the calibration procedure worked for the spectra. The same effect of the pulser remains after the DSP analysis (not shown in figure 48) and the order of the spectra on the plot remains the same. Moreover, one can observe the disappearance of the "unusual" peaks that were present after the DAQ analysis. They have been therefore caused by unfiltered waveforms. One more thing to observe is the higher count rate for the measurement on the aluminium contact, explained by the longer time exposure to the radiation source.

9 Conclusion and outlook

LEGEND will investigate the existence of the neutrinoless double beta decay in high purity ^{76}Ge detectors in its 200kg phase and also further with a better exposure by using a total detector mass of 1000kg.

This experimental test provided an insight into the functionality of semiconductor germanium detectors and the relationship of the physical side of the experiment to the electronics. The germanium detectors need to be operated carefully, at low temperatures, well calibrated and kept away from sources of noise, in order to yield correct physical results. The test of the high voltage contacts was motivated by the performance problems encountered by some detectors regarding energy resolution and the positions of the full energy peak and pulser. The result of this measurement yields that the quality of the high voltage contact is affecting the energy resolution of the detector.

As a conclusion, the high resistance on the high voltage contacts does not impact the spectrum histogram itself, with all high resistance contacts registering correct thorium spectra containing all fundamental peaks. However, the impact of a higher resistance reflects itself the reduction of the physical peak amplitude and degradation of energy resolution. Thus, the polished lithium contact presented the worst energy resolution because of having the highest resistance. The resistance of polished lithium contact has similar values to ones in LEGEND.

By performing this test and already observing differences between the contacts, one can conclude that the quality of high voltage contact exerts observable influence on the performance of the detector. The result regarding the shift of physical peak amplitude for the polished lithium contact directly proves the second statement of the scenario with a bad high voltage contact, where the n+ signal partly coupled to the p+ signal of the detector. It was observed that the peak amplitudes decreased compared with good contacts, because the negative signal coupled to the p+ contact partially cancelling the positive signal. This conclusion motivates follow-up measurements in this project, like the high voltage scans performed in LEGEND, but at a smaller scale, namely on the BEGe detector and in liquid nitrogen. Furthermore, this high voltage scan should be performed also in liquid argon, in order to clearly have the charge effects present to influence the surface of the detector and its electric potential. The experiments on one detector at the laboratory in Munich could shed light, if these effects also happen at a small scale.

References

- [1] *Particles and Nuclei, An Introduction to the Physical Concepts*, Seventh Edition, Bogdan Povh, Klaus Rith, Christoph Scholz, Frank Zetsche, Werner Rodejohann DOI:<https://doi.org/10.1007/978-3-662-46321-5>, Publisher Springer Berlin, Heidelberg, Hardcover, ISBN978-3-662-46320-8, Published: 25 June 2015
- [2] W. Pauli “*Pauli letter collection: letter to Lise Meitner*”. Typed copy. 1930. url: <https://cds.cern.ch/record/83282>
- [3] Wikipedia, <https://upload.wikimedia.org/wikipedia/commons/thumb/2/2b/RaE1.jpg/440px-RaE1.jpg>
- [4] C. L. Cowan et al. “*Detection of the Free Neutrino: a Confirmation*” In: *Science* 124.3212 (1956), pp. 103–104. issn: 0036-8075. doi: 10.1126/science.124.3212.103
- [4] Ivor Fleck, Maxim Titov, Claus Grupen, Irène Buvat, *Handbook of Particle Detection and Imaging* 2021, ISBN: 978-3-319-93784-7
- [5] Brookhaven National laboratory, <https://www.bnl.gov/bnlweb/history/nobel/1988.php>
- [6] Fermilab, <https://news.fnal.gov/2000/07/physicists-find-first-direct-evidence-tau-neutrino-fermilab/>
- [7] D.H. Perkins *Particle Astrophysics* Second Edition, ISBN:9780199545469
- [8] Masayuki Nakahata *History of Solar Neutrino Observations*, <https://doi.org/10.48550/arXiv.2202.12421>
- [9] N. Palanque-Delabrouille et al. “*Neutrino masses and cosmology with Lyman-alpha forest power spectrum*” In: *Journal of Cosmology and Astroparticle Physics* 2015.11 (Nov. 2015), pp. 011–011. doi: 10.1088/1475-7516/2015/11/011
- [10] Katrin collaboration, Karlsruhe Institute of Technology, <https://www.katrin.kit.edu/79.php>
- [11] The KATRIN Collaboration, *Direct neutrino-mass measurement with sub-electronvolt sensitivity* *Nat. Phys.* 18, 160–166 (2022). <https://doi.org/10.1038/s41567-021-01463-1>
- [12] Cattadori, C.M.; Salamida, F. *GERDA and LEGEND: Probing the Neutrino Nature and Mass at 100 meV and beyond*. *Universe* 2021, 7, 314. <https://doi.org/10.3390/universe7090314>
- [13] *The Physics of Neutrinoless Double Beta Decay: A Primer*, Ben Jones, arXiv:2108.09364v2[nucl-ex]25 Feb 2022
- [14] *The Large Enriched Germanium Experiment for Neutrinoless $\beta\beta$ Decay, LEGEND-1000 Preconceptual Design Report* URL: arXiv:2107.11462v1[physics.ins-det]23Jul2021
- [15] Matteo Agostini, Giovanni Benato, Jason A. Detwiler, Javier Menendez, Francesco Vissani, *Toward the discovery of matter creation with neutrinoless double-beta decay*, arXiv:2202.01787v2[hep-ex]10 Nov 2022

- [16] Hunklinger, Siegfried. *Festkörperphysik*, Berlin, Boston: De Gruyter Oldenbourg, 2018. <https://doi.org/10.1515/9783110567755>
- [17] F. Henkes, *Development and Characterization of novel readout electronics for LEGEND*
- [18] CUORE experiment collaboration, <https://cuore.lngs.infn.it/en/about/physics>
- [19] LEGEND collaboration, <https://legend-exp.org/science/neutrinoless-bb-decay/neutrinos-vs-no-neutrinos>
- [20] LEGEND collaboration, <https://legend-exp.org/science/legend-pathway/legend-200>
- [21] LEGEND collaboration, Michael Willers
- [22] F. Edzards, *Characterization of Point Contact Germanium Detectors and Development of Signal Readout Electronics for LEGEND*, <https://mediatum.ub.tum.de/?id=1609363>
- [23] University of Calgary, *Energy education* <https://energyeducation.ca/encyclopedia/Band-gap/>
- [24] ECStudioSystems, <https://ecstudiosystems.com/discover/textbooks/solid-state-devices/special-devices/zenner-diode/>
- [25] *Isotopically modified Ge detectors for GERDA: from production to operation*, URL: 2013 JINST 8 P04018 (<http://iopscience.iop.org/1748-0221/8/04/P04018>)
- [26] Physics Open lab, <https://physicsopenlab.org/2016/01/31/thorium-gamma-spectrometry/>
- [27] *Germanium* Britannica encyclopedic, <https://www.britannica.com/science/germanium>
- [28] Tobias Bode, *The neutrinoless double beta decay experiment GERDA Phase II: A novel ultra-low background contacting technique for germanium detectors and first background data*
- [29] G.F. Knoll, *Radiation Detection and Measurement*, 2010, Isbn: 9780470131480
- [30] David C. Radford, LEGEND Internal Call
- [31] M Agostini et al., »*Signal modeling of high-purity Ge detectors with a small read-out electrode and application to neutrinoless double beta decay search in Ge-76*«, in: *Journal of Instrumentation* 6.03 (2011), P03005–P03005, URL: doi: 10.1088/1748-0221/6/03/p03005
- [32] LEGEND Internal Call, slides
- [33] , *Handbook of Particle Detection and Imaging*, Second Edition, Ivor Fleck, Maxim Titov, Claus Grupen, Irène Buvat
- [34] George Terence Meaden, *Electrical Resistance of Metals*, 1965, Springer New York, NY

- [35] H. Fritzsche, *Electrical properties of germanium semiconductors at low temperatures*, Physical review, Volume 99, Chapter 2, 15 July 1955
- [36] B. Tapadia, *Low temperature resistivity of germanium semiconductor*, Faculty of the Department of electrical Engineering, University of Houston, 1970
- [37] LEGEND collaboration meetings and private conversations with LEGEND members
- [38] Samuel Joseph Meijer *Precision modeling of germanium detector waveforms for rare event searches*, University of North Carolina at Chapel Hill, 2019